New Journal of Physics
The open-access journal for physics

On the depinning of a driven drop on a heterogeneous substrate

Uwe Thiele[1,3] **and Edgar Knobloch**[2]

[1] Max-Planck-Institut für Physik komplexer Systeme, Nöthnitzer Str. 38, D-01187 Dresden, Germany
[2] Department of Physics, University of California, Berkeley, CA 94720, USA
E-mail: thiele@mpipks-dresden.mpg.de and knobloch@tardis.berkeley.edu

New Journal of Physics **8** (2006) 313
Received 24 April 2006
Published 11 December 2006
Online at http://www.njp.org/
doi:10.1088/1367-2630/8/12/313

Abstract. We study the depinning of driven drops on a heterogeneous substrate using a long-wave evolution equation for the film thickness profile. The heterogeneity is incorporated into an additional pressure term describing the interaction of the liquid with the substrate or with an external field. A drop may be pinned by a hydrophilic defect at the back or a hydrophobic defect at the front. Two types of depinning occur depending on the strength of the driving. The first occurs via a saddle-node (sniper) bifurcation, while the second involves a Hopf bifurcation. The parameter dependence of the depinning process is studied using linear stability theory, and direct numerical simulations are used to explore the dynamical properties of the stick-slip motion of the drop after depinning.

[3] Author to whom any correspondence should be addressed.

PII: S1367-2630(06)31574-1

Contents

1. Introduction

It is well known that liquid drops on an ideally smooth substrate move in response to external gradients. For example, a drop on an inclined substrate slides downslope in response to the gradient of potential energy [1]–[3]. Likewise a drop in a temperature gradient will move towards lower temperatures as a result of Marangoni forces caused by surface tension gradients [4, 5]. A wettability gradient induced by chemical grading of the substrate also causes drop motion: in order to minimize its energy the drop moves towards the most wettable region [6]–[9].

Although on ideally smooth substrates drops will move even for arbitrarily small gradients, this is not the case for the 'real' substrates used in experiments. There the onset of drop motion is strongly influenced by spatial heterogeneities such as wettability defects [8], [10]–[18], defects in the topography of the substrate or variations in the substrate temperature [19, 20]. For drops in a condenser [21, 22] spatial variations in the electric field act in much the same way as wettability defects [23]. In all these cases, a finite driving force is necessary to overcome the pinning influence of the heterogeneities [12, 14, 16], [24]–[27]. In addition, substrate heterogeneities can suppress the coarsening of arrays of droplets in the late stages of dewetting [28]–[30]. Indeed, heterogeneities occurring on a micro- or mesoscale are known to affect the macroscopic movement of drops and are responsible, for instance, for the observed hysteresis between advancing and receding contact angles [31]–[33], and the roughening of contact lines [31, 32], [34]–[36]. Another signature of substrate defects is the so-called stick-slip motion of weakly driven contact lines encountered, for instance, in the late stages of capillary rise [26, 37] or sessile drop experiments [38].

A common approach to drop pinning–depinning and the associated stick-slip motion is to regard the contact line motion as a transition between different metastable states as determined by

the minimization of appropriate energies [16, 17]. However, the resulting description is quasi-static and cannot account for the dynamics of the resulting stick-slip motion. In contrast, a dynamical model has to take into account not only the underlying energy landscape but also the dynamics of the relaxation towards the local minima. Other theories [27, 39] predict contact angle hysteresis without substrate heterogeneities but cannot account for stick-slip motion.

In this paper, we use a dynamical model to describe driven drops in a spatially heterogeneous system, and focus on understanding not only the processes that lead to pinning, but also the bifurcations that lead to depinning and the subsequent behaviour of a moving drop. Pinning and depinning transitions have, of course, been studied extensively in a variety of fields. The simplest situation is described by the Adler equation [40]

$$\dot{\theta} = \mu - \sin\theta, \tag{1}$$

where θ represents, for example, the drop position, and $\mu > 0$ measures the strength of the driving force. When $\mu < 1$ this equation has a pair of fixed points, one of which is stable and the other unstable. At $\mu = 1$ these fixed points annihilate in a saddle-node bifurcation, but unlike the standard saddle-node bifurcation this bifurcation produces periodic motion for $\mu > 1$. This result is simplest to understand if we write (1) as $\dot{\theta} = -\mathrm{d}V/\mathrm{d}\theta$, $V \equiv -\mu\theta - \cos\theta$. Evidently, (1) represents an overdamped particle in a cosinusoidal potential that is progressively tilted as μ increases. A 'particle' in a stable equilibrium at a local minimum of this potential 'spills out' once the tilt becomes large enough that its position no longer corresponds to a minimum. This occurs precisely at $\mu = 1$. The periodic motion present for $\mu > 1$ corresponds to the particle sliding down the resulting 'washboard' potential. It is important to note that the period of this motion diverges as $(\mu - 1)^{-1/2}$ [41]. The resulting bifurcation is sometimes called a Saddle-Node Infinite PERiod bifurcation, or 'sniper' for short.

Many depinning phenomena in physics may be understood using this simple picture. Usually this is so in systems with a continuous symmetry such as invariance under translations. In the absence of a heterogeneity spatially periodic structures may undergo a parity-breaking bifurcation that breaks the left–right symmetry of the pattern and produces a drift. The direction of the drift is determined by the associated tilt of the structure [42]. In this case, the drift speed of the structure vanishes as the square root of the distance from the parity-breaking bifurcation. However, in the presence of spatial heterogeneities the situation changes dramatically because near the bifurcation even small amplitude heterogeneities suffice to pin the tilted structure. A detailed study of this regime [43] shows that while some depinning events are indeed analogous to the behaviour described by the Adler equation, a quite different depinning mechanism is present as well. Here the tilted periodic state first undergoes a Hopf bifurcation that produces back-and-forth rocking motion of the tilted structure, but no net translation. As a parameter increases the amplitude of this oscillation increases leading to a global bifurcation involving an unstable fixed point and its translate by one period. This bifurcation generates oscillations with a nonzero mean drift, and this net drift increases with further increase in the parameter. In fact, the production of oscillations with net drift is a common consequence of global (or gluing) bifurcations. Other examples of global bifurcations leading to drift can be found in the theory of the Josephson junction [44] and in spiral wave convection [45]. In contrast, the pinning of fronts connecting homogeneous and structured states to the underlying structured state is described well by the sniper bifurcation [46, 47].

This paper is devoted to the understanding of the depinning transition in a simple dynamical model for driven liquid drops or ridges in a spatially heterogeneous system. We choose a generic

model describing driven drops on a solid substrate coexisting with a thin film or wetting layer [48], and introduce a heterogeneous interaction with the substrate with a well-defined spatial period. The heterogeneity might arise from chemical wettability defects, topographic defects or heterogeneous temperature or electric field. Random heterogeneities [34]–[36], [49] are not considered. The lateral driving might be caused by gravitational or centrifugal forces. Other possibilities include gradients of wettability, temperature or electric field.

We use lubrication theory and model the effect of heterogeneities through an additional spatially periodic pressure term. This term may consist of a disjoining pressure [30, 32, 48] modelling wettability or contributions that account for the influence of electric [21, 23] or temperature [50]–[52] fields, or a combination thereof. This dynamical approach has the advantage that drop shape and contact angles are not *a priori* set, and permits us to study the evolution of the shape and stability of a drop trapped by a heterogeneity as a function of the driving. Three cases are considered in detail: a periodic sinusoidal modulation of the pressure term, and strongly localized 'hydrophilic' or 'hydrophobic' defects. As a result, the drop may be pinned at the rear by a 'hydrophilic' region, or at its front by a 'hydrophobic' region. However, we do not seek an asymptotic description of macroscopic drops [9], focusing instead on the nature of the transitions involved in the process of depinning.

The paper is organized as follows. In the next section, we summarize the thin film model we use for the study of drop depinning. In section 3, we present the bulk of our results, and show that depinning occurs via both the sniper and Hopf bifurcations, and identify the conditions under which these mechanisms apply. These results are obtained by a combination of branch following methods, linear stability theory and direct numerical simulation of the model equation. Section 5 provides a brief outline of a theoretical understanding of the observed behaviour using a second order equation valid near a codimension-three point in parameter space. We also include a brief summary of the corresponding results for thicker films for which the corresponding flat film is metastable, i.e., no primary linear surface instability exists (section 6). All our calculations are two-dimensional. Our conclusions follow in section 7.

2. Model

A two-dimensional liquid layer on an inhomogeneous solid substrate subject to a lateral driving force of strength $\tilde{\mu}$ (figure 1) is modelled by an evolution equation for the film thickness profile $h(x, t)$ derived from the Navier–Stokes equation using the long-wave approximation [48]:

$$\partial_t h = -\partial_x \left\{ \frac{h^3}{3\eta} [\partial_x (\gamma \partial_{xx} h + P(h, x)) + \tilde{\mu}] \right\}. \tag{2}$$

Here γ is the surface tension, η is the dynamic viscosity, while $P(h, x)$ is an additional pressure term accounting for wettability, heating, electric field, etc [23]. As a particular example we employ a disjoining pressure describing wetting properties [32], [53]–[55], $P(h, x) = \kappa(bl^3/h^3 - \tilde{\xi}(x) \exp[-h/l])$, where κ is a typical energy density scale and the dimensionless coefficient $b > 0$ denotes the ratio of two antagonistic interactions. Our choice corresponds to a combination of long-range power law and short-range exponential interactions [53, 56, 57], with the spatial heterogeneity $\tilde{\xi}(x)$, i.e., the influence of wettability defects, contained in the short-range part. Some examples of the dimensionless form of $P(h)$ for a homogeneous substrate and the resulting stability diagram for a flat film are shown in figures 2(a) and (b), respectively.

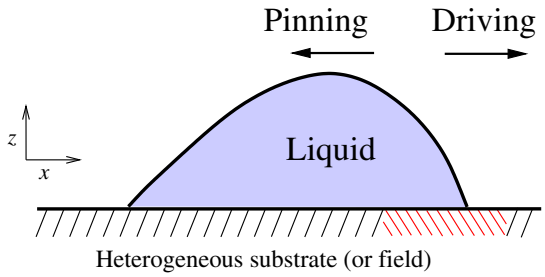

Figure 1. Sketch of a driven drop on a heterogeneous substrate.

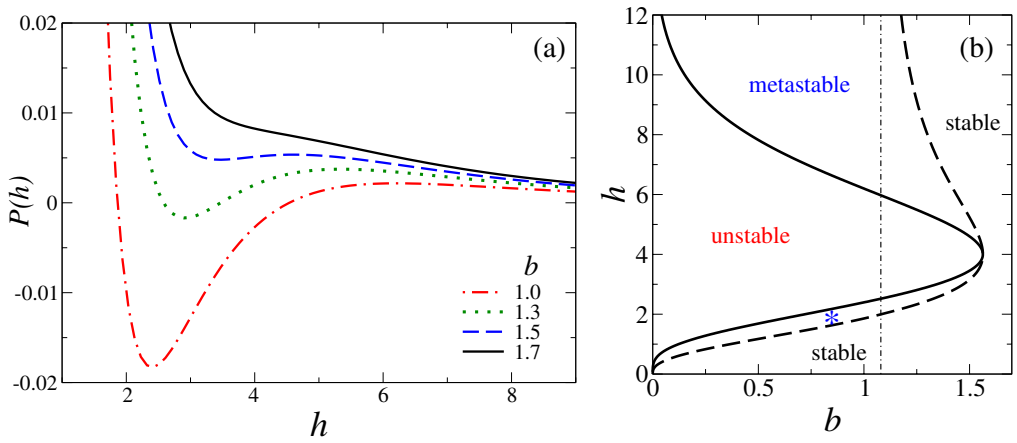

Figure 2. (a) The dimensionless pressure $P(h) = b/h^3 - \exp(-h)$ for several values of the parameter b. (b) The stability diagram for a flat film of thickness h in the (h, b) plane (after [57]). A star indicates the second metastable range while the vertical dot-dashed line shows the asymptote of the upper binodal line.

When $\tilde{\mu} = 0$ the resulting model allows for solutions representing static drops of arbitrarily large volume with a finite mesoscopic equilibrium contact angle sitting on a precursor film or wetting layer.

We nondimensionalize equation (2) using the scales $3\eta\gamma/\kappa^2 l$ for time and $\sqrt{l\gamma/\kappa}$ for the lateral coordinate. The film thickness is scaled by the interaction length l that provides a characteristic scale for the thickness of the wetting layer. The ratio of vertical and horizontal length scales $\sqrt{l\kappa/\gamma}$, i.e., the smallness parameter of the underlying lubrication approximation, is closely related but not equivalent to the equilibrium contact angle for drops on a homogeneous substrate, cf [9]. In addition, we define the dimensionless driving

$$\mu = \left(\frac{\gamma l}{\kappa^3}\right)^{1/2} \tilde{\mu} \tag{3}$$

standing, in general, for lateral forces that depend only weakly or not at all on film thickness like gravitational or centrifugal driving or a purely lateral temperature gradient. In the following the direction of driving and its opposite are called 'downstream' and 'upstream', respectively. We emphasize that any qualitatively similar pressure P yields like results, as shown for dewetting in [54], [57]–[61], heated wetting films in [51], and for chemically driven running drops in [62]–[64].

To uncover the details of the depinning transition it suffices to restrict attention to drops that are not much higher than the wetting layer. This case includes not only nano-drops on ultrathin precursor films ($l \approx 1 \ldots 10\,\mathrm{nm}$), where P only incorporates wetting properties, but also micro-drops on macroscopic wetting layers ($l \approx 10 \ldots 100\,\mu\mathrm{m}$). In the latter case P may include wettability in the form of repulsive van der Waals interactions together with the influence of temperature and/or electric field [23, 51, 52]. The case of drops in a condenser is illustrated in appendix A. The spatial modulation responsible for pinning can be included in any part of P. In the following, we call any heterogeneity that attracts (repels) liquid a 'hydrophilic' ('hydrophobic') defect. For instance, a warm (cold) spot on the substrate or a spot with lower (higher) voltage in a condenser would correspond to a 'hydrophobic' ('hydrophilic') defect [19].

In the following, we allow the short-range part of P to depend on the coordinate x,

$$\tilde{\xi}(x) = 1 + \epsilon\,\xi(x), \tag{4}$$

where $\xi(x)$ is a periodic function of x, and take

$$\xi(x) = \mathrm{sn}[4K(k)x/L_{\mathrm{het}}, k] \tag{5}$$

or

$$\xi(x) = \{2\mathrm{cn}[2K(k)x/L_{\mathrm{het}}, k]\}^2 - \Delta, \tag{6}$$

where $K(k)$ is the complete elliptic integral of the first kind and Δ is such that the average of $\xi(x)$ over a spatial period vanishes. The choice (5) allows us to vary the profile of the heterogeneity from sinusoidal, $\xi(x) = \sin(2\pi\, x/L_{\mathrm{het}})$ at $k = 0$, to a step profile as $k \to 1$, with hydrophilic and hydrophobic stripes of equal width. In contrast, (6) yields profiles with unequal widths: as $k \to 1$ (6) describes localized hydrophilic ($\epsilon < 0$) or hydrophobic ($\epsilon > 0$) defects. In the following it will be convenient to use the logarithmic measure $s \equiv -\log(1 - k)$ to quantify the resulting heterogeneity profiles.

The dimensionless film evolution equation then takes the form

$$\partial_t h = -\partial_x\{h^3[\partial_x(\partial_{xx}h + P(h, x)) + \mu]\}, \tag{7}$$

where P is the dimensionless pressure

$$P(h, x) = \frac{b}{h^3} - [1 + \epsilon\xi(x)]\,\mathrm{e}^{-h}. \tag{8}$$

In the absence of lateral driving, i.e., $\mu = 0$, one can assign an energy to every film profile $h(x, t)$ using the Lyapunov functional [30, 60]

$$F[h] = \int_0^L [\tfrac{1}{2}(\partial_x h)^2 + f(h, x) - C_1(h - \bar{h})]\,\mathrm{d}x, \tag{9}$$

where L is the system size, $\bar{h} \equiv \int_0^L h(x)\,\mathrm{d}x/L$ is the mean film thickness, $f(x, h) = -\int P(x, h)\,\mathrm{d}h$ is the local free energy, and C_1 is a Lagrange multiplier corresponding to mass conservation. The minima of this functional correspond to stationary solutions of equation (7), i.e., solutions of

$$\partial_{xx}h + P(h, x) + C_1 = 0. \tag{10}$$

In writing this expression, we have set the first integration constant C_0 to zero, as required by the symmetry of the problem with respect to reflection in x about a suitably chosen origin, determined by the form (5) or (6) of the heterogeneity. However, in a precursor film model with lateral driving, $\mu \neq 0$, this reflection symmetry is absent, and in general $C_0 \neq 0$. In this case profiles $h(x)$ that are stationary in the laboratory frame satisfy

$$\partial_{xxx} h + \partial_x P(h, x) + \mu + \frac{C_0}{h^3} = 0; \tag{11}$$

such profiles are accompanied by a nonzero flux of fluid through each spatial period. The resulting situation differs from slip models used to study drops of finite length with 'true' microscopic contact angles which permit a variational formulation. In these theories, the onset of depinning is determined by comparing energies of metastable states, but the subsequent dynamics requires the specification by hand of the contact angles at the front and back (for examples involving contact line motion on homogeneous substrates, see [65, 66]). This makes the slip ansatz problematic since for moving drops both contact angles are determined by an interplay between heterogeneity and driving.

3. Results

In the following, we focus on values of b for which the range of metastability extends to thick films, i.e., $b \lesssim 1.1$ (cf figure 2(b)). In this regime flattened (pancake) drops are unstable.

3.1. Unforced system

The solution structure of equation (7) with a sinusoidal wettability pattern and a disjoining pressure derived from diffuse interface theory [67] but no driving ($\mu = 0$) is extensively studied in [29, 30], focusing on the transition from long-time coarsening to pinning at the substrate heterogeneities that occurs with increasing heterogeneity strength or decreasing heterogeneity period. In contrast, the focus of the present paper is on the details of the depinning transition that occurs as the lateral driving increases.

We recall first that thin films on a homogeneous substrate with $\partial_{hh} f < 0$ are unstable. This instability is a long-wave instability and sets in when the system size or equivalently the spatial period L exceeds $L = L_c$. A supercritical bifurcation then produces a branch of periodic drop-like solutions for $L > L_c$. However, if the primary bifurcation at $L = L_c$ is subcritical such solutions extend to $L_s < L_c$, and connect to the flat film at $L = L_c$ via a branch of unstable nucleation solutions [2]. Solutions for different mean film thickness are shown in figure 3 in terms of their L^2 norm $||\delta h|| \equiv \sqrt{\int_0^L (h(x) - \bar{h})^2 \, \mathrm{d}x/L}$ and the relative energy per unit length $E \equiv F[h]/L - f(\bar{h})$ as a function of the domain length L. The primary instability is supercritical when the film is thin ($\bar{h} = 1.5$), but becomes subcritical in thicker films ($\bar{h} = 7$). For even thicker films ($\bar{h} = 15$) the flat film is linearly stable, and no primary bifurcation exists. However, the film is metastable and branches of drop and nucleation solutions exist for $L > L_s$.

In general one expects that these solutions persist on a substrate with weak wettability variation provided their period is compatible with the period L_{het} of the wettability pattern. These solutions can then be continued numerically towards stronger wettability variation. As

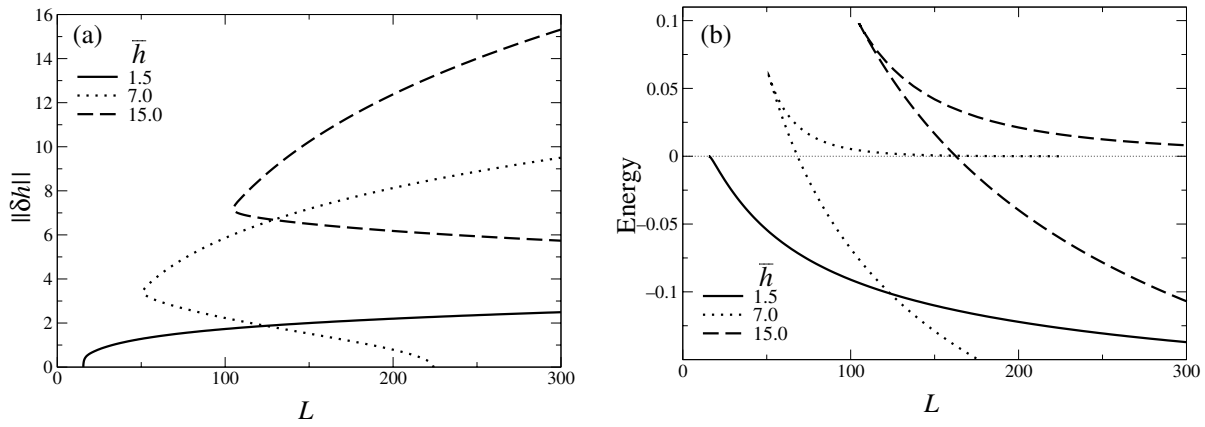

Figure 3. (a) The L^2 norm and (b) the energy E of solutions on a homogeneous substrate in the absence of driving, as a function of the spatial period L for $b = 0.1$ and mean thickness corresponding to linearly unstable ($\bar{h} = 1.5$, ——), subcritical ($\bar{h} = 7.0$, · · · · ·) and metastable flat films ($\bar{h} = 15.0$, – – –).

a result we expect solutions not only with $L = nL_{\rm het}$, $n = 1, 2, \ldots$ (studied in [30]), but also some that result from solutions on the homogeneous substrate with $L = L_{\rm het}/n$ for $n = 2, 3, \ldots$ and $L > L_{\rm c}$. Moreover, in the subcritical and metastable case $L > L_{\rm s}$, and additional solution branches result from the nucleation solutions [30]. For the wettability profiles (5) all of these branches come in pairs as ϵ splits the degeneracy between $h(x)$ and $h(x + L/2)$. Note that there is also one (nontrivial) solution branch corresponding to a flat film on a homogeneous substrate.

Figure 4 shows the solution families for a film on a substrate with a sinusoidal wettability pattern of period $L_{\rm het}$ and system size $L = L_{\rm het}$ in the absence of driving. Here, the critical period for instability is $L_{\rm c} = 15.5$. When $L = L_{\rm het} = 25$ the heterogeneity selects two branches from the circle of drop-like solutions (related by translations modulo the period) present when $\epsilon = 0$, one of which extends towards larger values of ϵ while the other annihilates with a branch arising from the uniform film solution ($||\delta h|| = 0$) on the homogeneous substrate. These branches all consist of a single drop per period. In contrast when $L = L_{\rm het} = 50$ branches of one, two and three drops per period are present, generated by the splitting of the corresponding solutions on the homogeneous substrate. As in the $L = L_{\rm het} = 25$ case these branches annihilate pairwise with increasing ϵ, leaving only the one-drop branch at larger heterogeneities. Examples of solutions on these branches are shown in figures 5(a) and (b). Figures 5(c) and (d) show the single drop profiles that survive to larger heterogeneities. We mention that on the smaller domain ($L = 25$) the mesoscopic contact angle increases with increasing amplitude of the heterogeneity, with the opposite trend for $L = 50$. Evidently, in the former case the drop is so large that it extends into the hydrophobic region and is therefore compressed, an effect that increases with ϵ. In contrast, on the larger domain the drop does not encroach on the hydrophobic area and so increasing ϵ lowers the mesoscopic contact angle.

The picture is qualitatively similar for non-sinusoidal wettability patterns, with one difference: if the wettability pattern breaks the symmetry $\epsilon \to -\epsilon$, $x \to x + L_{\rm het}/2$ the solutions will depend on the sign of ϵ and the corresponding branches become asymmetric with respect to $\epsilon = 0$. Figure 6 presents the overall characteristics of the families of solutions on heterogeneous substrates in the absence of driving. It gives results for different non-sinusoidal but symmetric

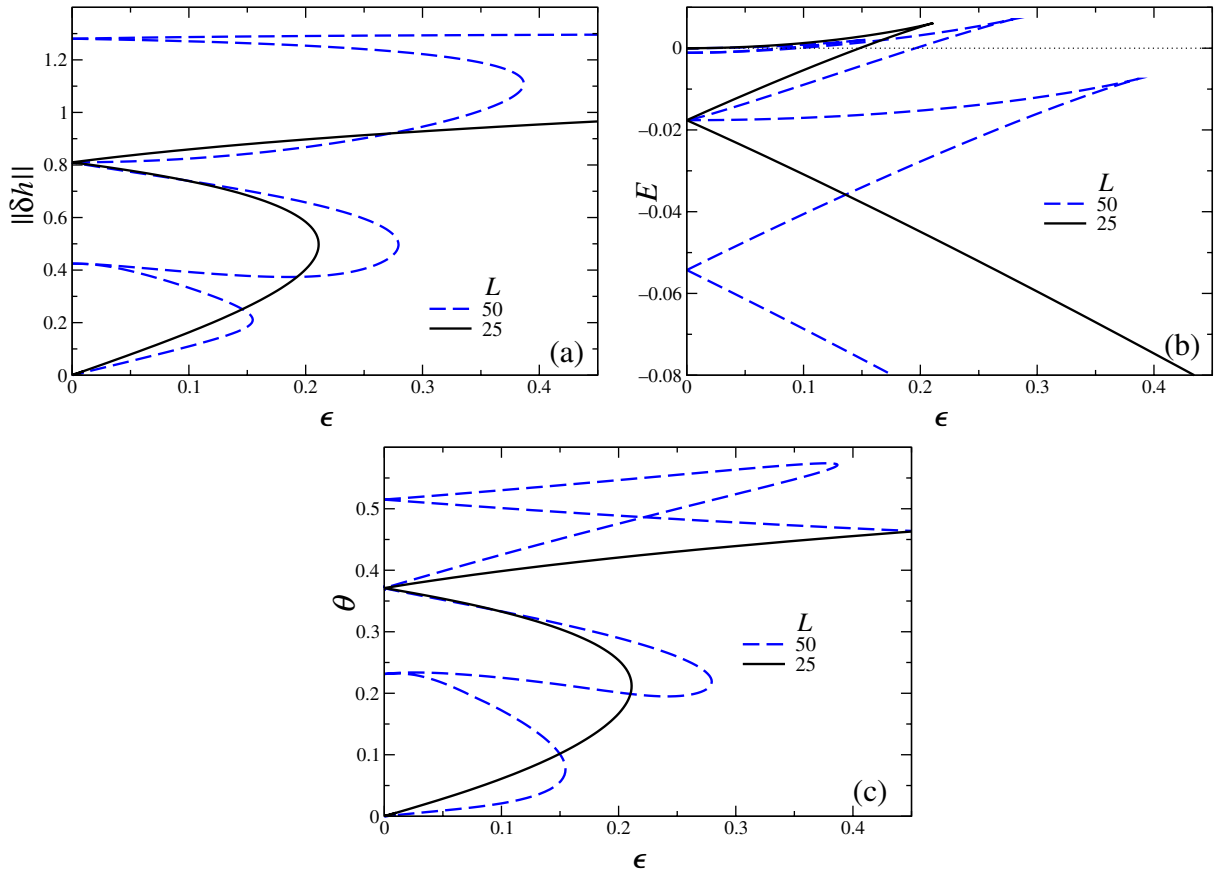

Figure 4. Solutions on a heterogeneous substrate in the absence of driving for a sinusoidal wettability pattern as a function of the wettability contrast ϵ for two different spatial periods L and $b = 0.1$, $\bar{h} = 1.5$. (a) L^2 norm; (b) energy E; (c) largest local slope of the profile θ (mesoscopic equilibrium contact angle). Only the highest lying states in (a) are stable. Thus the solid (dashed) lines in (a) have, from above, 0, 1, 2 (0, 1, 2, 3, 4, 5, 6) unstable eigenvalues.

wettability patterns with profiles given by equation (5), as well as for local wettability defects breaking that symmetry, given by equation (6).

3.2. Driven system

With lateral driving no steady drops exist on homogeneous substrates, i.e., substrates with no physical or chemical defect, and all drops slide with a velocity determined by the driving, liquid volume, wettability and the viscosity of the liquid. However, sliding drops that appear stationary in an appropriately moving frame, i.e., that slide without change of shape, are present [2, 68]. The situation changes on heterogeneous substrates where drops can be pinned by inhomogeneities. Pinning arises when the downstream driving force is balanced by an upstream force along the substrate generated by the gradient of $P(x)$. However, this balance requires the knowledge of both the drop shape and its position with respect to the heterogeneity. For very small driving

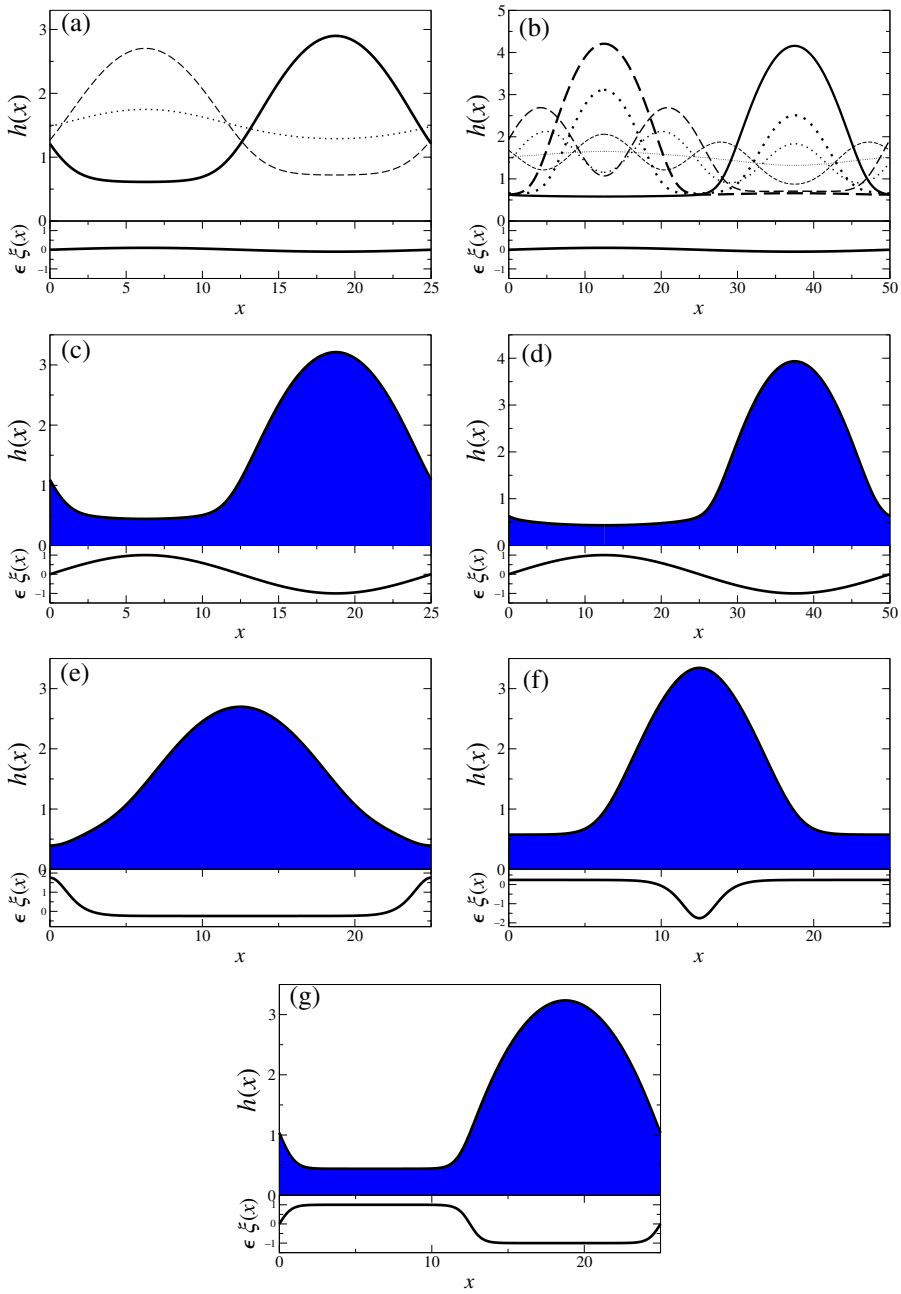

Figure 5. Steady film thickness profiles in the absence of driving for various wettability contrasts ϵ and system sizes $L = L_{\rm het}$. The upper and lower parts of each panel show the thickness profile $h(x)$ and the imposed wettability profile $\epsilon\xi(x)$, respectively. Panels (a) and (b) show all the steady profiles for $\epsilon = 0.1$ and $L = 25$ and $L = 50$, respectively. For a large heterogeneity ($\epsilon = 1.0$) only single drop profiles survive, as shown in (c) and (d) for $L = 25$ and $L = 50$, respectively. In (a)–(d) the wettability profile is sinusoidal; (e) and (f) are for non-sinusoidal asymmetric wettability profiles ($L = 25$, $s = 6$, equation (6)) with $\epsilon = \pm 1.0$, respectively. Finally, panel (g) shows the case of a non-sinusoidal symmetric wettability profile (5) for $L = 25$, $s = 6$ and $\epsilon = 1.0$. The remaining parameters are $b = 0.1$, and $\bar{h} = 1.5$.

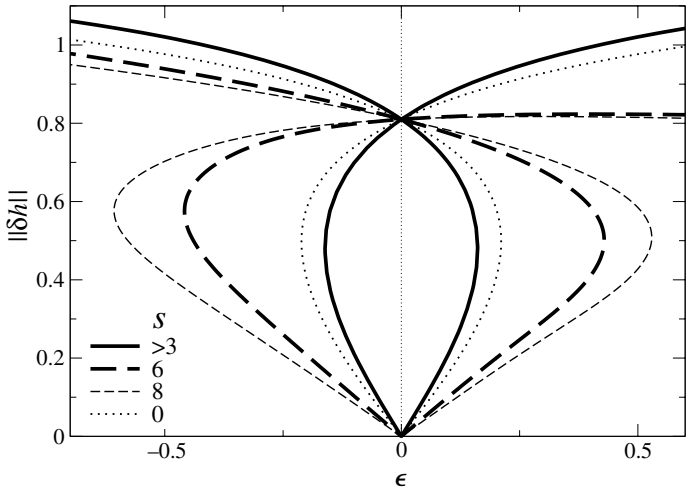

Figure 6. The L^2 norm of solutions on a heterogeneous substrate in the absence of driving for different non-sinusoidal wettability patterns characterized by s, as a function of the wettability contrast ϵ when $L = 25$, $b = 0.1$ and $\bar{h} = 1.5$. Solid (dashed) lines correspond to symmetric (non-symmetric) wettability patterns given by equations (5) ((6)). In the symmetric case the curves for different $s \geqslant 3$ cannot be distinguished by eye. The dotted line shows the sinusoidal case for comparison.

it is always possible to find such drop-like solutions. For larger driving, however, no stationary drops may exist and instead sliding drops or a flow with a stationary profile modulated by the heterogeneity will be present.

More complete information can be gathered by plotting families of stationary solutions as a function of the driving strength, as done in figure 7 for different wettability contrasts and heterogeneity profiles. Three main types of such families can be distinguished. (i) A monotonic transition with increasing μ between drop-like and film-like states, as occurs, for example, in figure 7(b) for $\epsilon = 0.5$. (ii) A non-monotonic transition between these states with increasing or decreasing μ, with multiple solutions present for $\mu_{\rm sn2} < \mu < \mu_{\rm sn1}$, as in figure 7(a) for $\epsilon = 0.5$. (iii) A discontinuous case, consisting of three branches. Of these the branches of drop-like and nucleation solutions terminate at a finite $\mu_{\rm sn1}$ in a saddle-node bifurcation, while the third branch consisting of film-like states is disconnected and exists for all μ. Consequently as μ increases one finds an abrupt transition from drop-like to film-like states, although the reverse transition is absent. An example is given by the $\epsilon = 0.2$ curve in figure 7(a) or the $\epsilon = \pm 0.4$ curves in figures 7(c) and (d).

The above discussion ignores the stability of these branches. One finds that for the supercritical values of L considered here the film-like state is always unstable, and hence the transition at the rightmost saddle-node necessarily leads to a time-dependent state. This is the depinning transition that is of particular interest in the present paper.

3.3. Linear stability of the steady states

Figure 8 shows representative drop profiles for different values of μ covering the range from $\mu = 0$ to the value where the drop depins (solid lines). Panel (a) shows the case of a hydrophilic

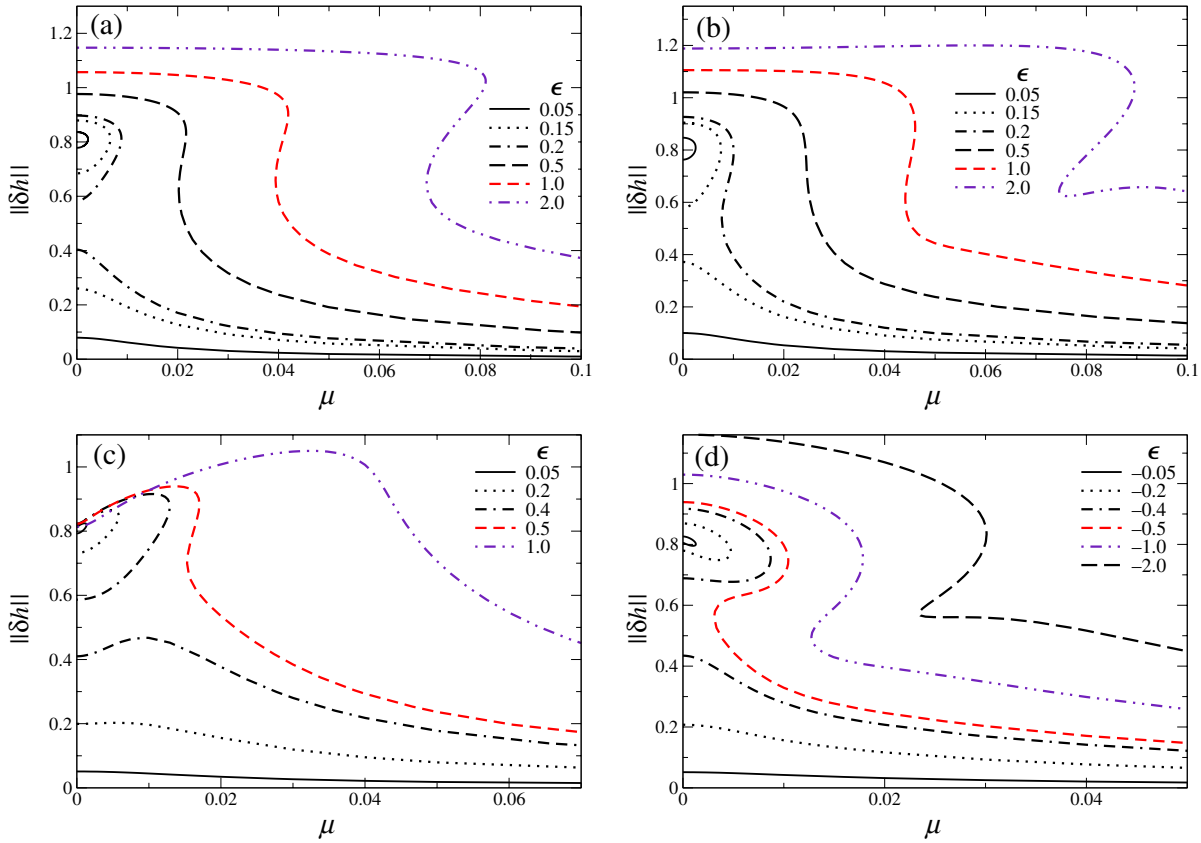

Figure 7. The L^2 norm of steady solutions on a heterogeneous substrate as a function of the applied driving μ for different wettability contrasts ϵ as given in the legend, and $L = 25$, $b = 0.1$, $\bar{h} = 1.5$. (a) Sinusoidal wettability pattern. (b) Non-sinusoidal symmetric wettability pattern given by equation (5) with $s = 6$. Non-symmetric wettability patterns given by equation (6) with $s = 6$ and (c) $\epsilon > 0$, (d) $\epsilon < 0$.

defect that holds the drop at its upstream end, leading to the formation of a prominent shoulder immediately prior to depinning. As this occurs the downstream (advancing) contact angle decreases, while the upstream (receding) angle also decreases, as the drop stretches markedly in extent. Panel (b) studies the influence of a hydrophobic defect that blocks the drop at its downstream end and leads to a strong increase of the downstream (advancing) contact angle. The upstream (receding) angle also increases as the drop becomes more and more compressed.

To determine the nature of the transition leading to depinning, we must examine the linear stability properties of the profiles $h_0(x)$ shown in figure 8. For this purpose, we linearize the evolution equation (7) about $h_0(x)$ and look for perturbations of the form $h_1(x, t) = h_1(x) \exp(\beta t)$. This procedure leads to the eigenvalue problem $\beta h_1(x) = \mathbf{L}[h_0(x)]h_1(x)$ for the growth rates β and the associated instability modes $h_1(x)$. Note that $\mathbf{L}$ depends nonlinearly on h_0 and its derivatives (for a detailed example related to front instabilities see [69]). The solution of this problem yields the spectrum of eigenvalues as a function of the driving strength μ. Figure 9 shows the result for a sinusoidal heterogeneity corresponding to particular branches in figure 7(a).

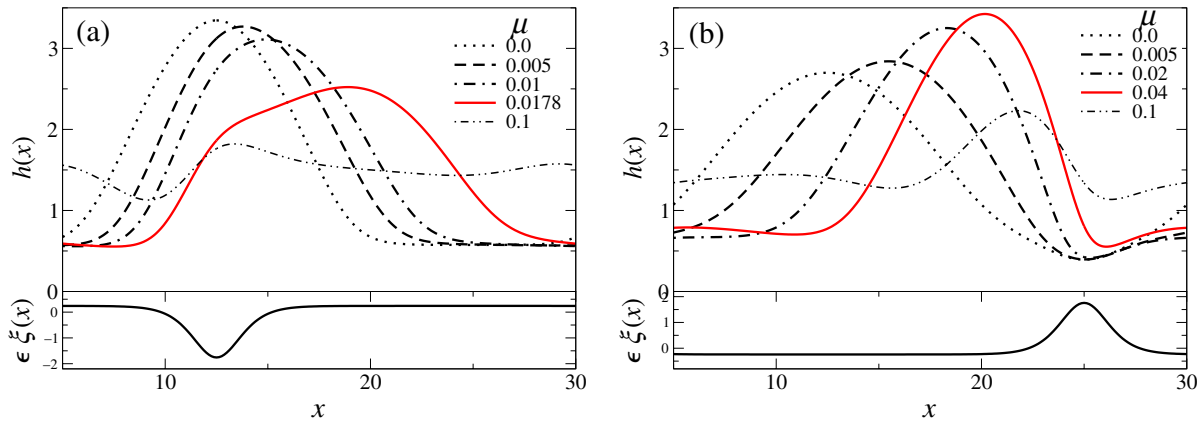

Figure 8. Thickness profiles of stationary solutions on a heterogeneous substrate with the profile (6) for different values of μ and $L = 25, b = 0.1, \bar{h} = 1.5, s = 6$. In (a) the wettability contrast is $\epsilon = -1$, i.e., the movement of the drop is hindered by a hydrophilic patch underneath, whereas in (b) $\epsilon = 1$ and the drop is pinned by a hydrophobic patch in front of it. The plots for $\mu = 0.1$ are for the (unstable) steady flowing film coexisting with the time-dependent state after the drop depins. The profile at depinning is shown as a solid line (red online).

When these are discontinuous only the results for the branch of drop-like solutions are shown. For small values of the heterogeneity amplitude ϵ the upper drop-like state remains stable until the first saddle-node bifurcation where a real eigenvalue becomes positive (figures 9(a) and (b)). For larger ϵ some of the real eigenvalues collide pairwise and move into the complex plane (figure 9(b)). In this case only the real part of the complex pair is shown; such complex eigenvalues are indicated by dashed lines. For yet larger ϵ a pair of saddle-node bifurcations appears on the solution branch forcing the leading eigenvalues to undergo a 'drunken dance' as a function of μ. This is a consequence of the fact that at each saddle-node a real eigenvalue must pass through zero. Figure 9(c) shows that the collision of the two unstable real eigenvalues on the film-like portion of the solution branch leads to a pair of complex eigenvalues with positive real part, reflecting the oscillatory instability of the film-like portion of the branch at larger μ. For yet larger ϵ complex eigenvalues appear even on the upper drop-like portion of the branch (figure 9(d)), but this branch remains stable until the saddle-node bifurcation. As a result the leading complex eigenvalues must become real prior to the saddle-node bifurcation (figure 9(d)). Note that despite the presence of complex eigenvalues loss of stability (i.e., depinning) occurs via saddle-node bifurcations where a real eigenvalue passes through zero.

The situation becomes more interesting when the heterogeneity is non-symmetric as shown for a hydrophobic defect in figure 10. For moderate values of the wettability contrast ϵ (figure 10(a)) depinning continues to occur via a saddle-node bifurcation. However, with increasing ϵ these saddle-nodes annihilate in a so-called hysteresis bifurcation (figure 7), and the eigenvalues are no longer forced to become real. In this case a new phenomenon arises: the drop-like solutions on the upper branch lose stability at a Hopf bifurcation (figure 10(b)). Thus, in this case, the pinned drops start to 'rock' prior to the depinning transition. The nature of the depinning transition must therefore be quite different from the case where depinning occurs

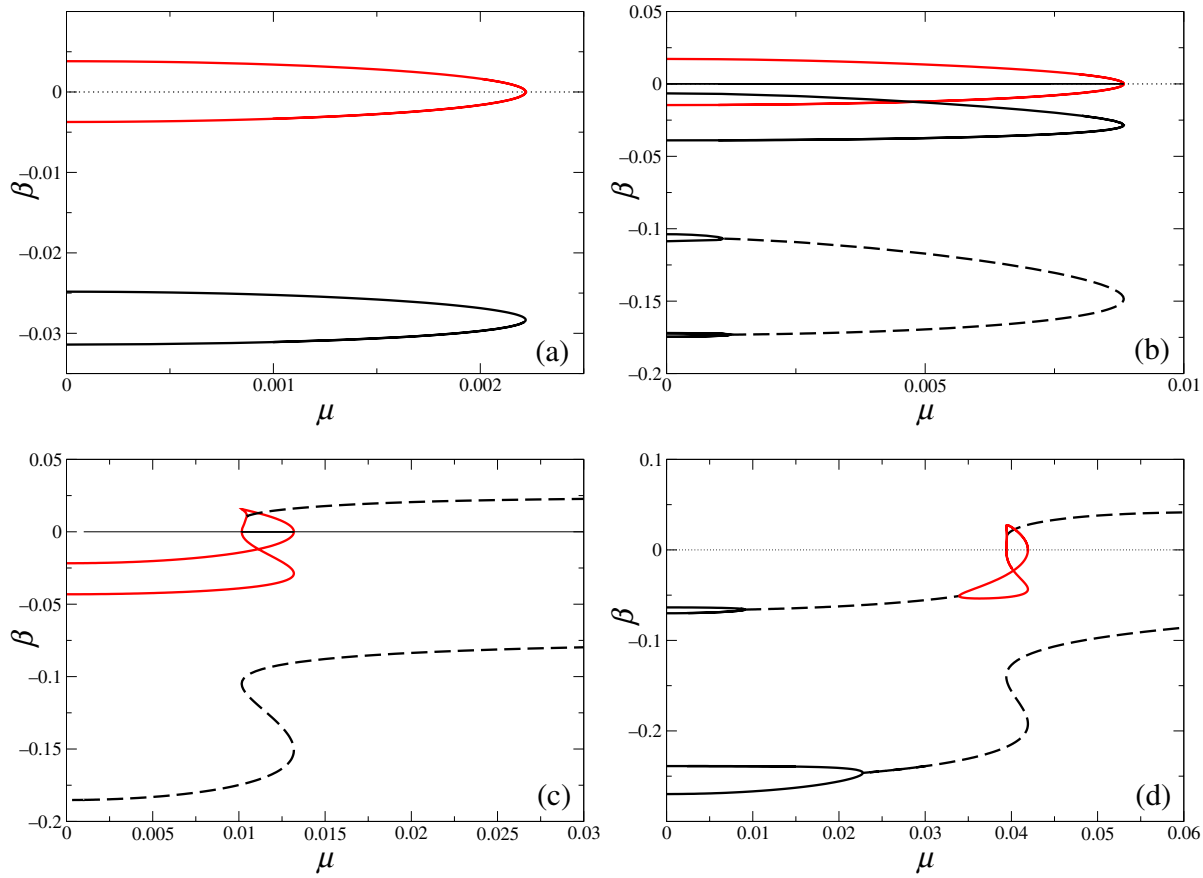

Figure 9. Stability of steady solutions on a heterogeneous substrate with a sinusoidal wettability pattern (cf figure 7(a)) as a function of μ. Shown are the leading eigenvalues β for different wettability contrasts ϵ and $L = 25$, $b = 0.1$, $\bar{h} = 1.5$. (a) $\epsilon = 0.05$, (b) $\epsilon = 0.2$, (c) $\epsilon = 0.3$, and (d) $\epsilon = 1.0$. Real (complex) eigenvalues are shown as solid (broken) lines.

at a saddle-node bifurcation. Also of considerable interest is the behaviour of the eigenvalues past the Hopf bifurcation ($\mu > \mu_{\mathrm{H}}$): with increasing ϵ an interval of μ values appears with real eigenvalues (figure 10(c)), and these come closer and closer to the Hopf bifurcation as ϵ increases (figures 10(c)–(e)) and eventually result in a pair of saddle-node bifurcations (figure 10(f)). However, the Hopf bifurcation remains.

It is significant that one of the real eigenvalues involved in this process increases very abruptly with μ. This behaviour reflects the sudden and abrupt loss of stability once the drop depins, and indicates that the drop accelerates rapidly from its equilibrium state prior to depinning, in accord with everyday observation.

The nature of the depinning process is captured in the eigenfunctions responsible for the loss of stability, i.e., the eigenfunctions at the onset of depinning, as well as the eigenfunctions associated with the large growth rates identified in figure 10. In figure 11(a), we show the eigenmode corresponding to a close to maximum (real) growth rate in figure 10(e). The mode peaks in the downstream direction of the drop, and has a prominent dip on the upstream side

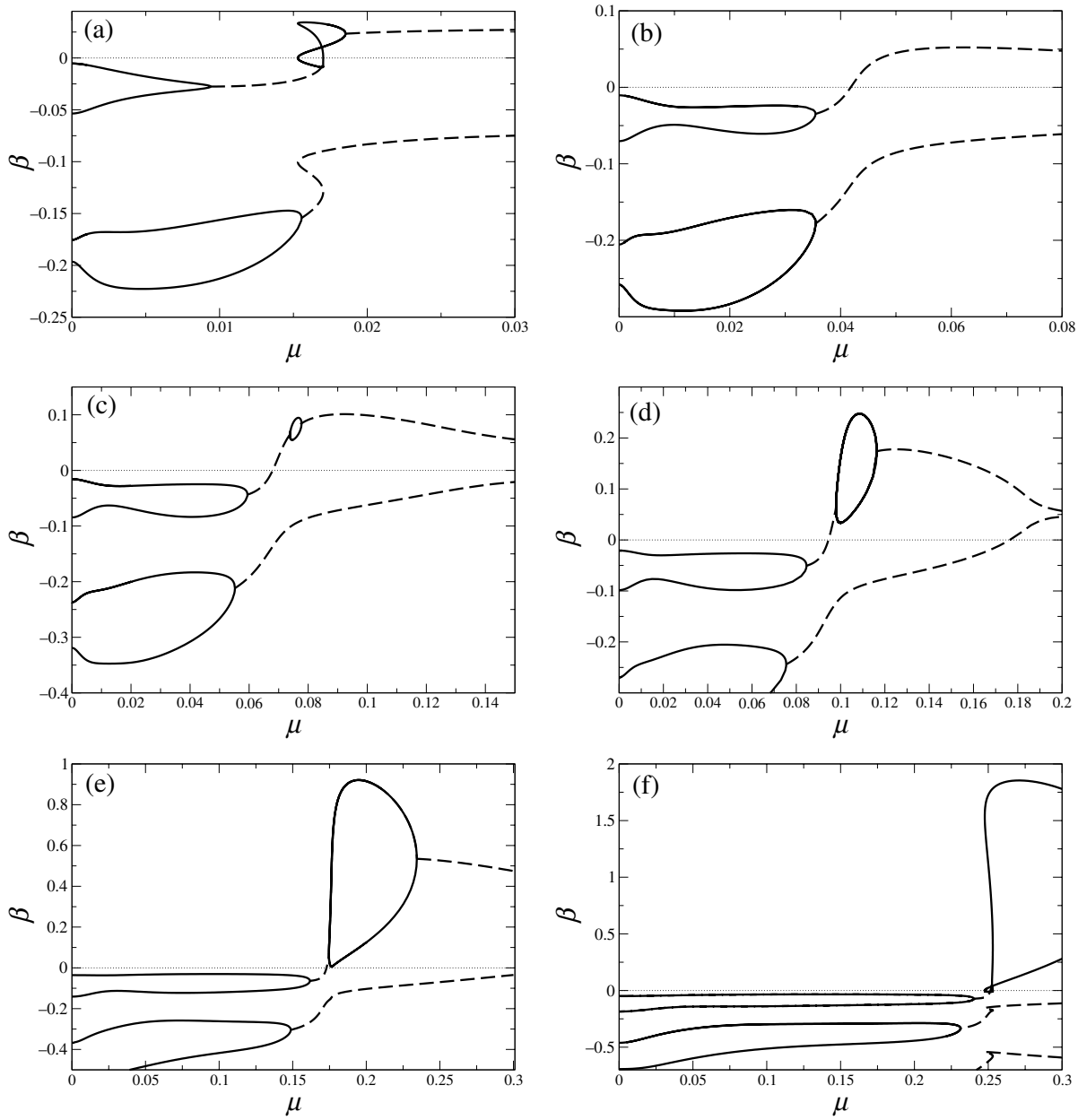

Figure 10. Stability of steady solutions on a heterogeneous substrate with a localized hydrophobic defect (cf figure 7(c)) as a function of μ. Shown are the leading eigenvalues for different wettability contrasts ϵ and $L = 25$, $b = 0.1$, $\bar{h} = 1.5$, $s = 6$. (a) $\epsilon = 0.5$, (b) $\epsilon = 1.0$, (c) $\epsilon = 1.5$, (d) $\epsilon = 2.0$, (e) $\epsilon = 3.5$, and (f) $\epsilon = 5.0$. Real (complex) eigenvalues are shown as solid (broken) lines.

of the drop apex, clearly indicating that the loss of stability is associated with the transfer of liquid from the upstream to the downstream side, in other words, that the instability produces downstream motion. Indeed, the mode resembles in form the function $h_0'(x)$ that corresponds to the translation mode on a homogeneous substrate. In contrast, figure 11(b) shows the oscillatory eigenmode at the first Hopf bifurcation in figure 10(d). Like the real eigenmode in figure 11(a)

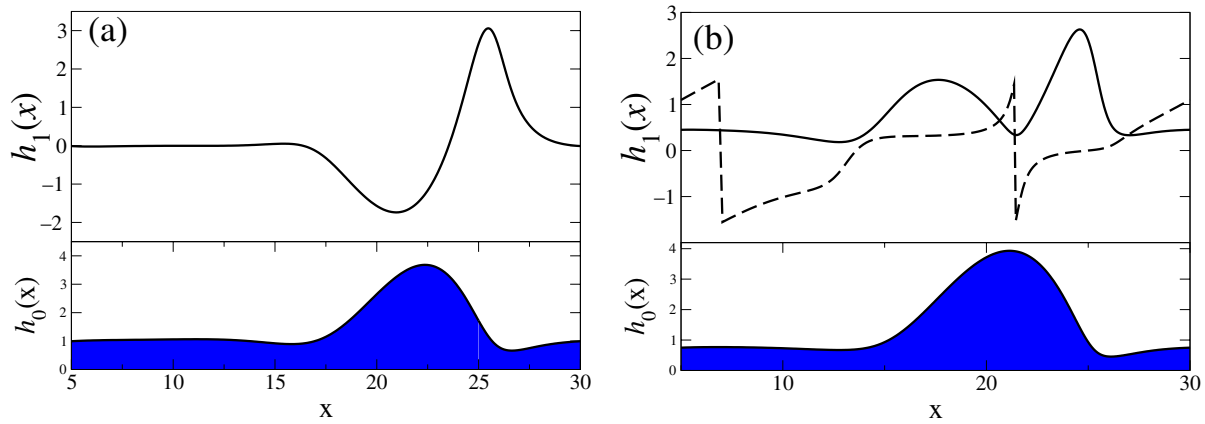

Figure 11. Instability modes for steady solutions on a heterogeneous substrate with a non-sinusoidal hydrophobic defect (cf figure 7(c)) for $L = 25$, $b = 0.1$, $\bar{h} = 1.5, s = 6$ and several values of the driving strength μ and wettability contrast ϵ: (a) $\epsilon = 3.5$, $\mu = 0.2$ (real mode), (b) $\epsilon = 2.0$, $\mu = 0.094$ (complex mode). The upper panels show the leading eigenmode (solid line: absolute value; broken line: phase) while the lower panels show the corresponding steady drop profile.

the modulus of the associated complex mode $|h_1(x)|$ also peaks on the downstream side of the drop. On the other hand, there is a secondary (albeit smaller) maximum on the upstream side, suggesting the onset of asymmetric rocking motion of the drop. This motion is visible in the perturbation $|h_1(x)|\ \cos(\beta_i t + \phi(x))$ of the steady profile $h_0(x)$ shown in figure 12(b) in the form of a space-time plot. Figure 12(c) shows that farther from onset the rocking becomes more nonuniform and that its maximum amplitude moves downstream, while figure 12(d) shows the behaviour associated with the second Hopf mode that sets in at $\mu \approx 0.18$ (see figure 10(d)). Finally, figure 12(a) shows the behaviour at the Hopf bifurcation in figure 10(b).

Figures 13 and 14 summarize the location of the saddle-node bifurcations μ_{sn1}, μ_{sn2} in the (μ, ϵ) plane (heavy lines), together with the location of both primary and secondary Hopf bifurcations (dashed lines). The shaded regions correspond to three equilibria; only one equilibrium is present outside these regions. The regimes where stable pinned drops are present are indicated; these lose stability at a saddle-node bifurcation across the heavy line, and at a Hopf bifurcation across the dashed line. Note that contrary to appearance the line of Hopf bifurcations does not emerge from the cusp where the two saddle-node bifurcations annihilate. The figures also show that for a sinusoidal defect the saddle-nodes persist with increasing ϵ, and no Hopf bifurcations are present.

Figure 15 shows the contact angles at the front and back of the pinned drop as a function of increasing driving strength μ. In the following we refer to these as the advancing and receding (equilibrium) angles, respectively. For a drop pinned at the back (left) the advancing (receding) angle decreases (increases) for small but increasing μ (figure 15(a)). However, once the drop starts developing a shoulder at the back the receding angle decreases again until depinning occurs (at a saddle-node bifurcation). The situation is different for a drop pinned at the front (right). In this case both angles increase with μ almost until depinning but drop just prior to it (figure 15(b)). The only decrease in the receding angle occurs at very small driving.

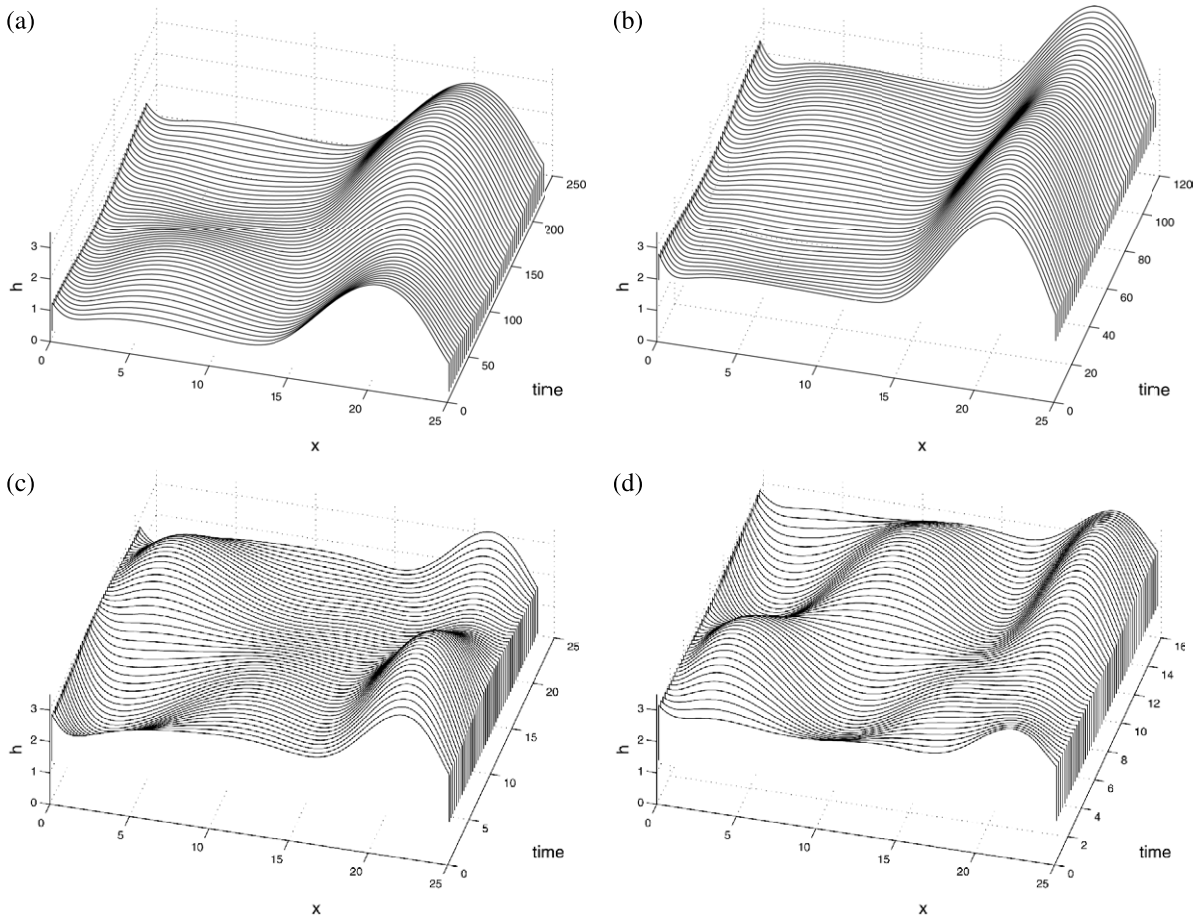

Figure 12. Visualization of the oscillatory instability modes. Shown are space-time plots of the steady profile together with a superposed disturbance of amplitude $a = 0.1$: $h(x, t) = h_0(x) + a\,|h_1(x)|\,\cos(\beta_i t + \phi(x))$. (a) $\epsilon = 1.0$, $\mu = 0.042$, $\beta_i = 0.028$ (at the Hopf bifurcation); (b) $\epsilon = 2.0$, $\mu = 0.0945$, $\beta_i = 0.054$ (at the primary Hopf bifurcation); (c) $\epsilon = 2.0$, $\mu = 0.16$, $\beta_i = 0.30$ (beyond the primary Hopf bifurcation); (d) $\epsilon = 2.0$, $\mu = 0.18$, $\beta_i = 0.41$ (at the secondary Hopf bifurcation). The remaining parameters are $L = 25$, $b = 0.1$, $\bar{h} = 1.5$, and $s = 6$ (heterogeneity given by equation (6)).

The advancing and receding angles at depinning shown in figure 16 provide a measure of the contact angle hysteresis observed macroscopically. In the case of a hydrophobic defect at the front ($\epsilon > 0$) both angles increase nearly linearly, and continue to do so even for oscillatory depinning ($\epsilon \gtrsim 0.6$); the small hook visible in the figure near this transition is consistent with the fact that the Hopf bifurcation sets in prior to the disappearance of the saddle-node bifurcations. The behaviour is more intricate when the pinning is by a hydrophilic defect at the back ($\epsilon < 0$). In this case the role of the two angles is reversed, and both decrease nearly linearly with slopes identical to those in the $\epsilon > 0$ case. For $\epsilon \lesssim -0.2$, however, the receding angle reverses tendency and starts to increase again, while the advancing angle continues to decrease. This qualitative change in behaviour is similar to that occurring with increasing driving in figure 8(a): the force drags the main body of liquid downstream but the spot of higher wettability traps part of it upstream. For fixed μ the latter effect becomes more pronounced as $|\epsilon|$ increases.

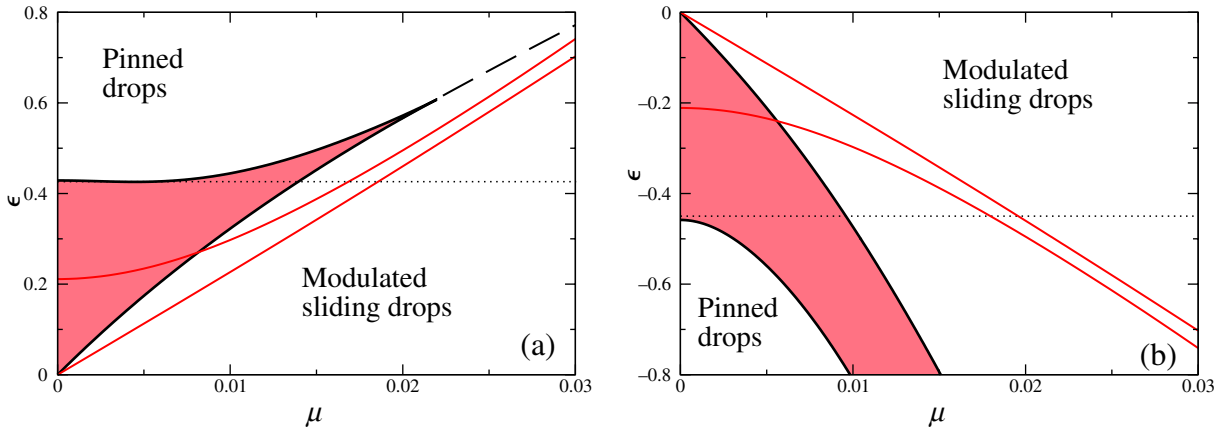

Figure 13. Phase diagram for depinning of driven drops on a heterogeneous substrate with a non-sinusoidal wettability pattern given by equation (6) with $s = 6$, and $L = 25$, $b = 0.1$, $\bar{h} = 1.5$. The figure focuses on small wettability contrast as measured by the parameter ϵ for (a) a less wettable defect, and (b) a more wettable defect. The thick solid (dashed) lines correspond to saddle-node (Hopf) bifurcations. The latter emerge near the cusp at which the two saddle-node bifurcations in (a) annihilate. Note that in the former case the saddle-node bifurcations disappear with increasing driving μ, while in the latter case the saddle-nodes appear to persist for all μ. The thin lines show the corresponding results for a sinusoidal wettability pattern.

4. Unsteady states

In this section we describe the results obtained from solving the time-dependent problem (7), (8) for different choices of the wettability pattern $\xi(x)$, focusing on the dynamics that result from the depinning transition. We write the partial differential equation for the film thickness profile as a system of coupled ordinary differential equations for the film thickness at equidistant points in space, and impose periodic boundary conditions in space. The system is integrated in time using an explicit variable order, variable time step Adams method (NAG library routine 'd02cjc' [70]). Simulations are either started from slightly perturbed flat films or from steady solutions at nearby parameter values. After an initial transient the profiles settle down on a steady state or approach a time-periodic state.

4.1. Sinusoidal heterogeneity

The pinned states for a sinusoidal wettability profile are studied in figure 7(a). Figure 9 shows that depinning occurs via a saddle-node bifurcation and that beyond depinning the growing eigenmode becomes oscillatory if the wettability amplitude ϵ and hence μ at depinning are large enough. In figure 17, we show space-time plots of time-dependent solutions of (7), (8) corresponding to figure 9(d) for (a) $\mu = 0.042$ and (b) $\mu = 0.08$. Both motions are strictly periodic in time. The former is very close to the depinning transition, at a value of μ for which the resulting motion has a very large period. The figure shows that the drop remains near equilibrium for an extended period before showing a slight drift in the downstream direction. This drift then accelerates

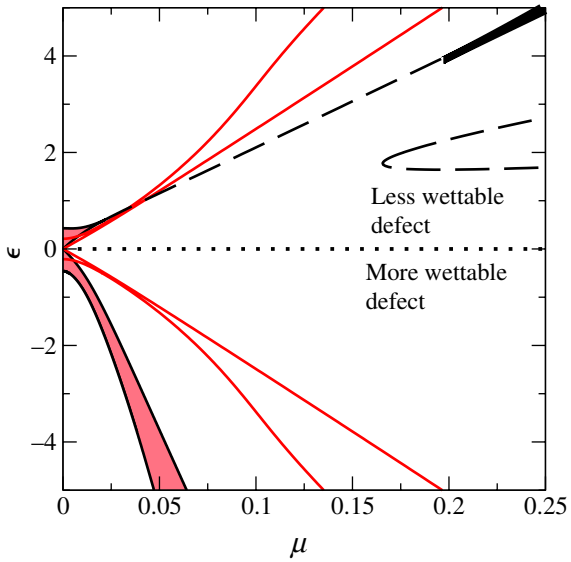

Figure 14. As in figure 13 but spanning a larger range of wettability contrasts and driving strengths μ. The thin lines correspond to a sinusoidal wettability pattern and are symmetric with respect to $\epsilon = 0$. Note the reappearance of saddle-node bifurcations at large driving and wettability contrasts $\epsilon > 0$ (cf figure 7(b)). The second dashed line indicates Hopf bifurcations related to a secondary eigenvalue.

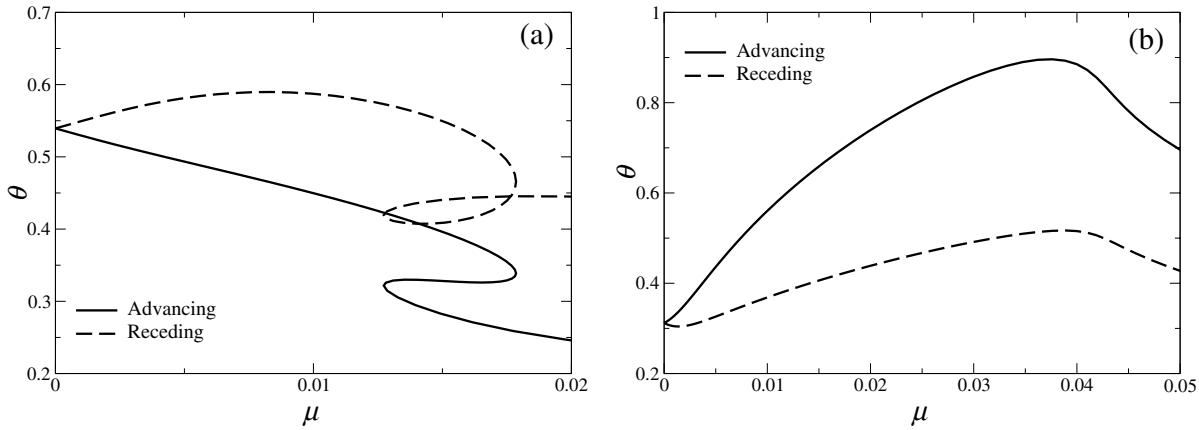

Figure 15. Advancing and receding equilibrium contact angles θ of a pinned drop as a function of the driving strength μ for (a) a hydrophilic defect with $\epsilon = -1$, and (b) a hydrophobic defect with $\epsilon = 1$, both for $L = 25$, $b = 0.1$, $\bar{h} = 1.5$, $s = 6$ (heterogeneity given by equation (6)).

rapidly as the drop translates to the vicinity of the next equilibrium position one spatial period ahead. The overall dynamics resembles stick-slip motion. Figure 17(b) shows the corresponding behaviour farther from the depinning transition, i.e., for a larger driving strength μ. We see that the drop leaves the defect position more rapidly, and thins down as it flows to the next defect position. The dynamics is more fluid, and no longer resembles stick-slip motion.

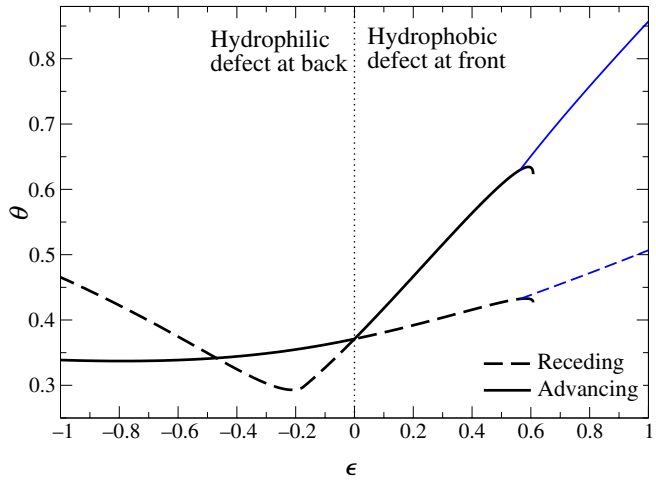

Figure 16. Advancing (solid lines) and receding (broken lines) contact angles θ at the depinning transition for varying wettability contrast for a hydrophilic defect at back ($\epsilon < 0$) and hydrophobic defect at front ($\epsilon > 0$), both for $L = 25$, $b = 0.1$, $\bar{h} = 1.5$, $s = 6$ (heterogeneity given by equation (6)). Thick (thin) lines refer to depinning through a real (oscillatory) mode.

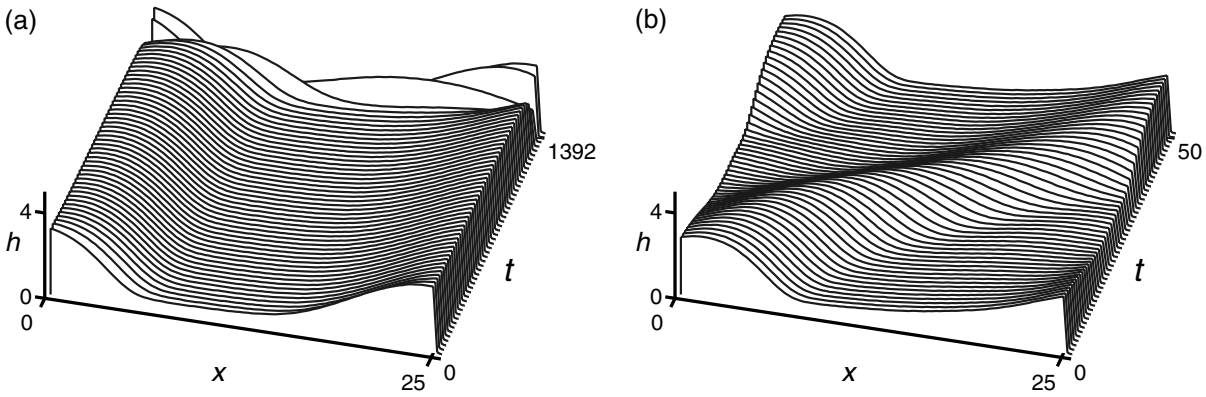

Figure 17. Time evolution of sliding drops beyond depinning from a sinusoidal heterogeneity. Shown are space-time plots over one period in space and time (a) close to depinning at $\mu = 0.042$ with a temporal period of $T = 1392$, and (b) far from depinning at $\mu = 0.08$ with $T = 50$. The remaining parameters are $L = 25$, $b = 0.1$, $\bar{h} = 1.5$ and $\epsilon = 1.0$.

Figure 18 extends the above results to different values of μ. We see that in terms of $||\delta h||$ the time for the drop to leave the defect position as μ becomes larger becomes comparable to the time it takes to return to such a position. As a result the depinning becomes less sudden. The same trend is revealed when we track the location of the maximum height of the drop (figure 18(b)). The figure shows that in all cases the maximum moves downstream, rather abruptly for μ close to the depinning transition, more slowly for large μ. The vertical jumps in

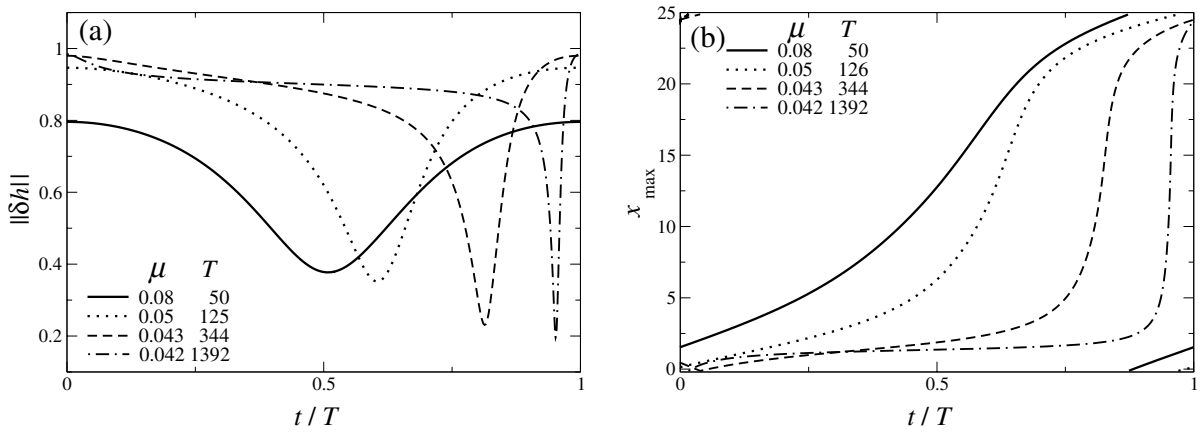

Figure 18. Characteristics of sliding drops beyond depinning from a sinusoidal heterogeneity for various μ. (a) The L^2 norm and (b) the position of the global maximum over one temporal period T. The remaining parameters are as in figure 17, with identical conditions at $t = 0$.

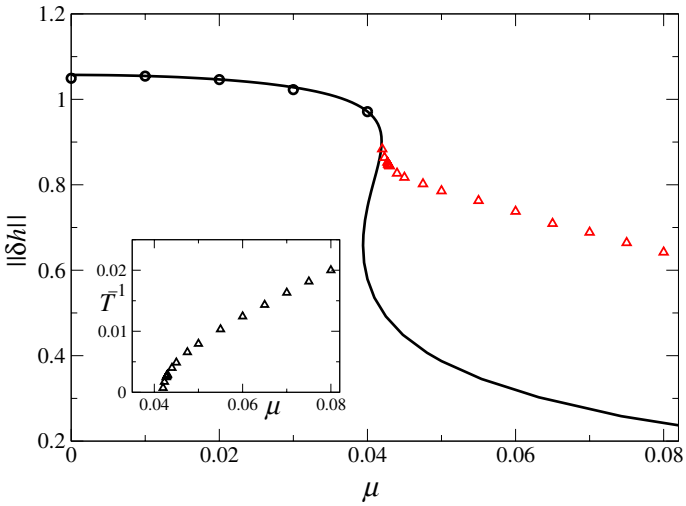

Figure 19. Bifurcation diagram for the depinning transition from a sinusoidal heterogeneity with $\epsilon = 1.0$ and $L = 25$, $b = 0.1$, $\bar{h} = 1.5$, showing the L^2 norm for the branch of steady solutions (——), selected steady solutions as obtained by direct integration in time (○) and the time-averaged L^2 norm for the unsteady solutions beyond the depinning bifurcation (△). The inset shows the inverse temporal period for the latter.

the figure indicate that the drop has moved one spatial period, and the motion continues with $x_{\max}$ at $x = 0$.

Figure 19 shows a bifurcation diagram presenting on the same plot the norm $||\delta h||$ for the equilibria (figure 7(a)) and the time average of this quantity for the time-dependent states after depinning. The figure shows that these time-dependent states do indeed bifurcate from

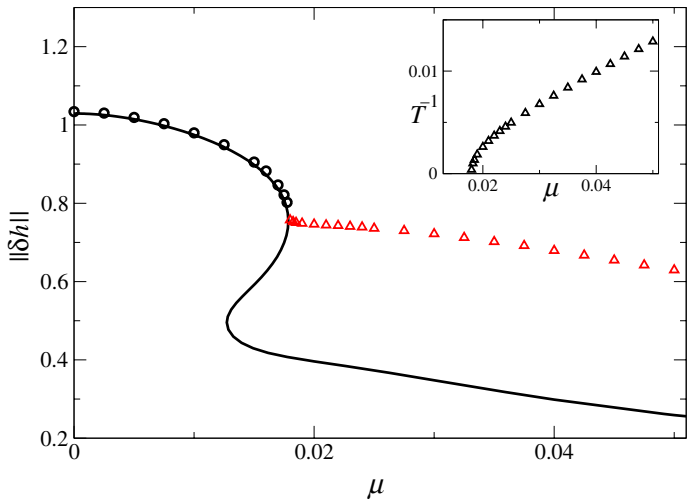

Figure 20. Bifurcation diagram for depinning via a sniper bifurcation from a hydrophilic defect with $\epsilon = -1.0$ and $L = 25$, $b = 0.1$, $\bar{h} = 1.5$, showing the L^2 norm for the branch of steady solutions (——), selected steady solutions as obtained by direct integration in time (○) and the time-averaged L^2 norm for the unsteady solutions beyond the depinning bifurcation (△). The inset gives the inverse temporal period for the latter. The heterogeneity is given by equation (6) with $s = 6$.

the saddle-node in a sniper bifurcation, and confirms that the period of the resulting periodic motion does diverge as the inverse square root of the distance from depinning as in the Adler equation (1).

4.2. Hydrophilic defect

As shown in figure 13(b) depinning from a hydrophilic defect also occurs via a sniper bifurcation. It is not surprising therefore that the qualitative results for this case resemble those for the sinusoidal wettability profile. Figure 20 shows a typical bifurcation diagram: the large amplitude drop-like states remain stable until a saddle-node bifurcation at which the drop depins and periodic stick-slip motion ensues. The period of this motion diverges as $(\mu - \mu_c)^{-1/2}$.

Figure 21(a) shows the dynamics of the profile for μ beyond depinning. The figure confirms that for μ near critical the translation of the drop occupies a much smaller fraction of the period than for larger driving. Figure 21(b) shows these results in a different form by focusing on the motion of the global maximum in height. The figure shows that near the end of the rapid sliding phase the global maximum switches to the location of the defect; this maximum moves slowly downstream under the influence of loading from an upstream drop, before triggering another sliding event. The figure also shows that for larger driving strength the global maximum moves at an essentially constant rate as the height of the perturbation due to the presence of the defect becomes less and less important. These properties of the solutions are clearly visible in the space-time plots shown in figure 22.

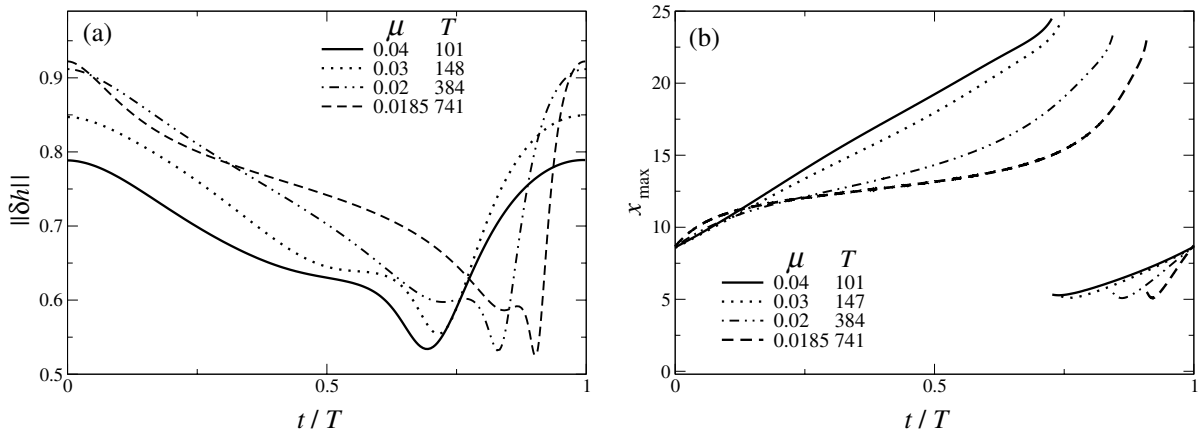

Figure 21. Characteristics of sliding drops beyond depinning from a hydrophilic defect via the sniper bifurcation for various values of μ as given in the legend, showing (a) the L^2 norm, and (b) the position of the global height maximum over one temporal period. The discontinuities in (b) reflect a switch in dominance between two local maxima. The remaining parameters are as in figure 20.

4.3. Hydrophobic defect

As already mentioned the hydrophobic heterogeneity permits a distinct mechanism for depinning. In this case, linear theory shows that the static drop may lose stability at a Hopf bifurcation as the driving strength μ increases. Figure 23 shows the drop profiles in a space-time plot at four values of μ beyond the depinning transition $\mu_{\rm H}$. In this case the frequency at onset remains finite, and figure 23(a) shows that near $\mu_{\rm H}$ the drop spends a long time near its equilibrium configuration before an abrupt translation to its next equilibrium position takes place. As expected the time spent near the defect position decreases with increasing μ, so much so that figure 23(d) shows a drop travelling at almost constant speed, only slightly modulated by the heterogeneity. Figure 24 shows these results in a different but more quantitative form. The figure shows that the position of the global maximum changes discontinuously at two points indicating that some liquid remains trapped behind the defect.

Figure 25(b) shows the norm $||\delta h||$ of the static pinned drop as a function of μ obtained by continuation (solid line) and compares the result with those obtained by numerical simulation of (7) and (8) in time (circles); triangles are used to indicate the time-averaged amplitude of the oscillatory states that result from depinning. The figure suggests that the Hopf bifurcation is in fact slightly subcritical. As a result we cannot follow the branch of time-dependent solutions all the way to the Hopf bifurcation.

It should be mentioned that with both increasing and decreasing ϵ the branch of static drops develops a pair of saddle-node bifurcations via a hysteresis bifurcation (figures 13 and 14). However, in both cases the Hopf bifurcation occurs above the upper saddle-node bifurcation. With decreasing wettability contrast the Hopf bifurcation moves towards this bifurcation, and disappears on colliding with it. Thus the oscillatory instability disappears in a Bogdanov bifurcation. This Bogdanov bifurcation is non-standard, however, since it involves the collision of a Hopf bifurcation not with a saddle-node but a sniper. This is because the spatial periodicity of the problem requires that the problem be posed in a phase space that is a cylinder (see section 5).

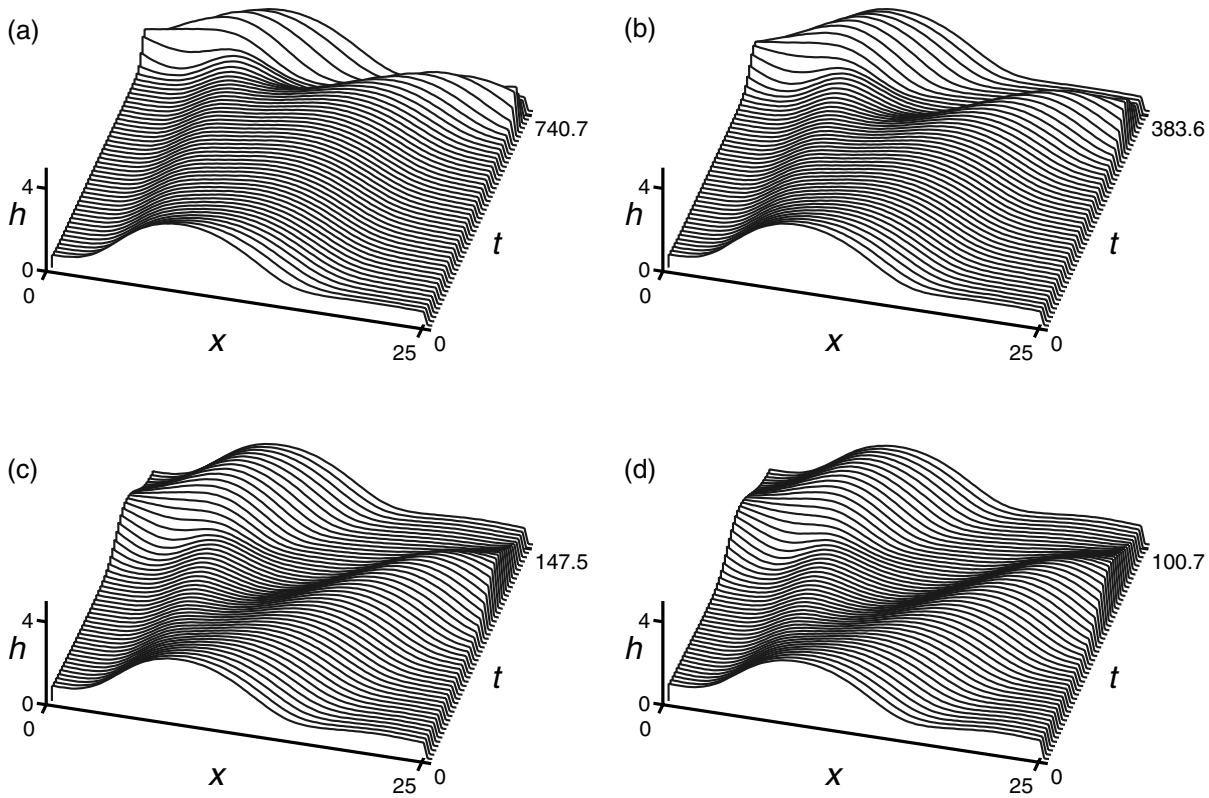

Figure 22. Time evolution of sliding drops beyond depinning via a sniper bifurcation in the form of space-time plots for one period in space and time. (a) Close to depinning at $\mu = 0.0185$ with a temporal period of $T = 740.7$, (b) at $\mu = 0.02$ with $T = 383.6$, (c) at $\mu = 0.03$ with $T = 147.5$, and (d) far from depinning at $\mu = 0.04$ with $T = 100.7$. The remaining parameters are as in figure 20. The time $t = 0$ corresponds to $t = 0$ in figure 21.

For smaller wettability contrasts depinning occurs via the sniper bifurcation, as shown in figure 25(a) for $\epsilon = 0.4$.

4.4. Dependence on loading

Finally, we also explore the dependence of the depinning transition on the loading of the defect. We use the spatial period L as a measure of the volume of liquid in the system, and hence of the amount of liquid that has to be held in the pinned state. Figure 26 shows the loci of the sniper bifurcation for a slightly hydrophobic defect in the (μ, L) plane. The figure shows that as the loading L increases the driving strength μ at which depinning occurs decreases ($\mu \sim L^{-1}$, at large L), and that μ is smaller for smaller wettability contrast. The presence of the cusps is notable, and indicates very high sensitivity of the driving strength at depinning to the loading in this regime. When L is too small (for the present parameter values $L \lesssim 20$, a value that depends only weakly on the wettability contrast) no drops form, and instead the solution takes the form of a thin but stationary film whose thickness is modulated by the underlying heterogeneity.

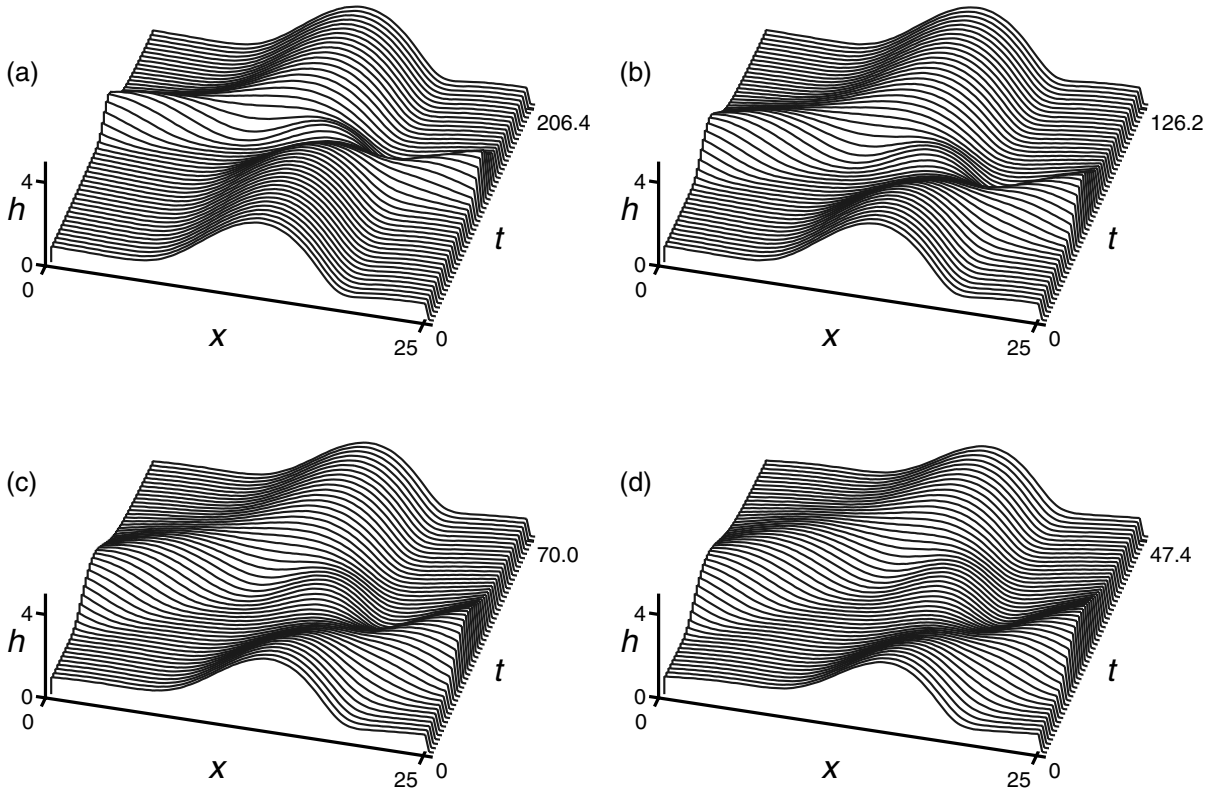

Figure 23. Time evolution of sliding drops beyond depinning via a Hopf bifurcation in the form of space-time plots over one period in space and time. (a) Close to depinning at $\mu = 0.0414$ with a temporal period of $T = 206.4$, (b) at $\mu = 0.045$ with $T = 126.2$, (c) at $\mu = 0.06$ with $T = 70.0$, and (d) far from depinning at $\mu = 0.08$ with $T = 47.4$. The remaining parameters are $L = 25$, $b = 0.1$, $\bar{h} = 1.5$, $\epsilon = 1.0$; the heterogeneity is a hydrophobic defect given by equation (6) with $s = 6$. The time $t = 0$ corresponds to $t = 0$ in figure 18.

5. Depinning mechanism

The depinning transitions via the sniper and Hopf bifurcations interact in parameter space near the location where the two saddle-nodes annihilate. In this region the Hopf bifurcation interacts with one of the saddle-node bifurcations producing the codimension-two Bogdanov bifurcation; in addition the second saddle-node is annihilated by the first in a hysteresis bifurcation, indicating that a third parameter must be tuned as well. Thus it is natural to consider a codimension three point in parameter space where the two saddle-nodes annihilate and at the same time interact with a Hopf bifurcation with zero frequency. The vicinity of this codimension-three point provides the key to the various transitions observed in our computations. These are captured by the system

$$\ddot{\theta} + \nu\dot{\theta} + A\sin\theta\dot{\theta} + \mu + \lambda\sin\theta + \sin^3\theta = 0, \tag{12}$$

where $A > 0$ is a constant, and the parameters ν, μ and λ are unfolding parameters and hence small. Here the variable θ is a periodic variable representing for example the behaviour of the

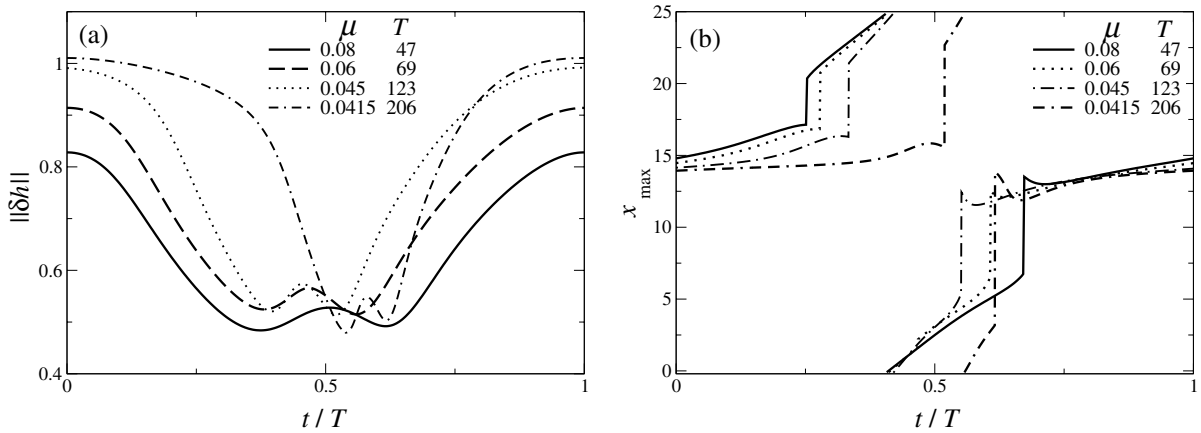

Figure 24. Characteristics of sliding drops beyond depinning via a Hopf bifurcation for various values of μ. (a) L^2 norm of δh. (b) Position of the global maximum over one temporal period. The remaining parameters are as in figure 23.

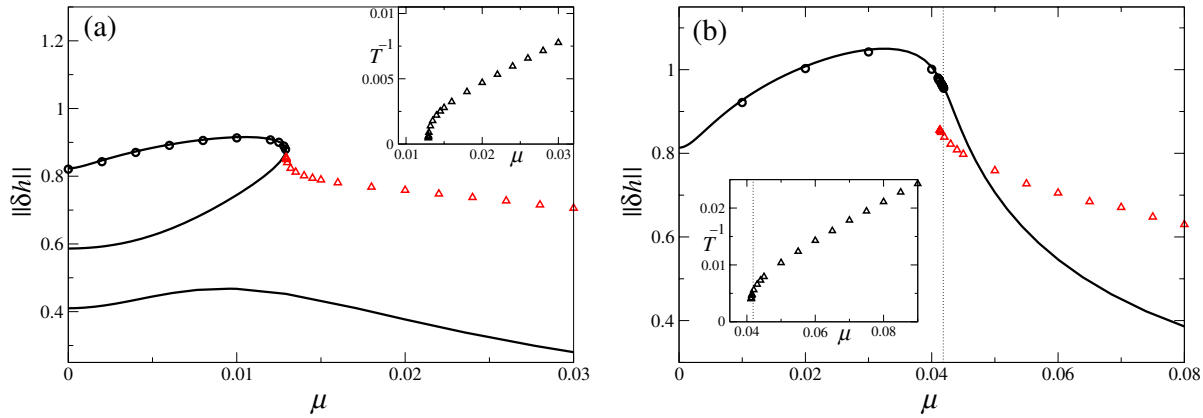

Figure 25. Bifurcation diagrams for depinning from a hydrophobic defect of type (6) with $s = 6$ and $L = 25$, $b = 0.1$, $\bar{h} = 1.5$. Depinning occurs in (a) via the sniper bifurcation for small wettability contrasts ($\epsilon = 0.4$) and in (b) via an oscillatory instability for larger wettability contrasts ($\epsilon = 1.0$, cf figure 10(b)). Line styles and inset are as in figure 20.

maximum of the film profile modulo the spatial period L of the system. Since μ and λ are small the equilibria of interest will have small θ. Consequently we may locally replace equation (12) by

$$\ddot{\theta} + \nu\dot{\theta} + A\theta\dot{\theta} + \mu + \lambda\theta + \theta^3 = 0. \tag{13}$$

In this equation it is helpful to think of θ as $\mathcal{O}(\epsilon)$, and take the time derivative to be also $\mathcal{O}(\epsilon)$, while $\nu = \mathcal{O}(\epsilon)$, $\mu = \mathcal{O}(\epsilon^3)$ and $\lambda = \mathcal{O}(\epsilon^2)$. Of these we think of ν, λ as fixed, and take μ as the distinguished bifurcation parameter; this parameter plays the role of the driving strength, and increases through zero from left to right with $\mu = 0$ at the codimension-three point.

In the following we denote the equilibria by θ_0, and note that there may be as many as three. These annihilate pairwise in saddle-node bifurcations at $\lambda + 3\theta_0^2 = 0$, and the saddle-node

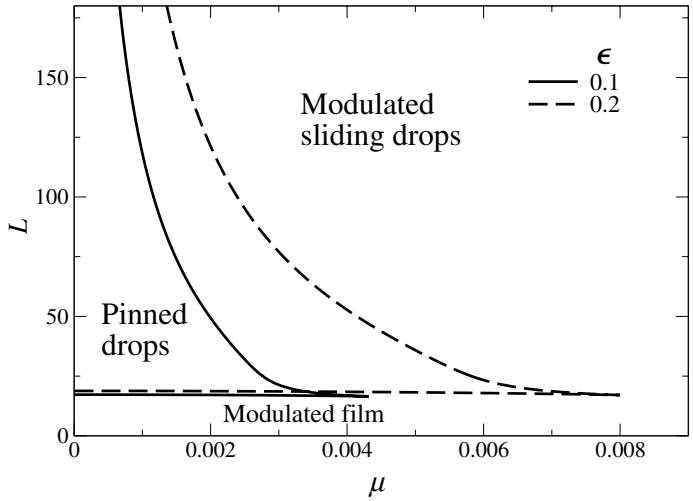

Figure 26. Loci of the sniper bifurcation in the plane spanned by the driving strength μ and the spatial period L that is a convenient measure for the volume in the pinned state. Shown is the case of pinning by a hydrophobic defect for two values of ϵ and $b = 0.1$, $\bar{h} = 1.5$. The heterogeneity is given by expression (6) with $s = 6$.

bifurcations themselves annihilate at $\mu = \lambda = 0$. Thus three equilibria are present for $\lambda < 0$ and one for $\lambda > 0$. Of these the leftmost equilibrium is stable. When $\lambda < 0$ a real eigenvalue passes through zero at the rightmost saddle-node bifurcation, followed by a further loss of stability at the leftmost saddle-node. Thus the rightmost equilibrium is always doubly unstable. When $\lambda > 0$ the stability assignments for large $|\mu|$ are preserved but since no saddle-node bifurcations are present it follows that the change in stability must occur via a Hopf bifurcation. To understand how the latter fits into the picture we examine the stability of the equilibria in more detail.

The linear stability of these is given by the eigenvalue equation

$$s^2 + (\nu + A\theta_0)s + (\lambda + 3\theta_0^2) = 0. \tag{14}$$

Steady state bifurcations ($s = 0$) correspond to the saddle-node bifurcations already mentioned; a Hopf bifurcation ($s = \pm i\omega$) occurs when $\nu + A\theta_0 = 0$ and requires $\lambda + 3\theta_0^2 > 0$. The latter condition is satisfied in the region $\lambda + 3\nu^2/A^2 > 0$, i.e., for $\lambda < 0$. The Hopf bifurcation has zero frequency when $\lambda + 3\theta_0^2 = 0$. Thus the curve $\lambda + 3\nu^2/A^2 = 0$ represents the location of the Bogdanov bifurcations. The corresponding values of the bifurcation parameter μ follow from $\mu + \lambda\theta_0 + \theta_0^3 = 0$. Note that the Bogdanov bifurcation coincides with the annihilation of the saddle-nodes only when $\nu = 0$; when $\nu > 0$ the Bogdanov bifurcation occurs on the lower equilibrium branch and vice versa. The calculation presented in figure 13 indicates that the value of ν in our problem is quite small; the degenerate Hopf bifurcation ($\omega = 0$) almost coincides with the cusp at which the saddle-node bifurcations annihilate.

Equation (12) can be used to follow the solutions of equation (13) away from $\mu = 0$, $\lambda = 0$. One finds that as μ increases for $\lambda < 0$ the rightmost saddle-node bifurcation is indeed a sniper, provided that $\nu > 0$. This bifurcation produces a limit cycle that is a rotation, i.e., θ advances by 2π each period. In contrast, the Hopf bifurcation creates oscillations with no net change in θ in one period. Oscillations of this type correspond to libration. Since sliding motion

necessarily corresponds to rotations, it follows that a global bifurcation must take place that changes librations into rotations; such a bifurcation must involve an unstable fixed point. In the case with only one fixed point the most likely candidate for such a bifurcation involves the collision of the zero-mean oscillation with the now unstable fixed point. Such a global bifurcation requires a three-dimensional system, however, and hence cannot occur within (12). It does occur in other systems such as the Takens–Bogdanov bifurcation with O(2) symmetry [71], case $II-$.

6. Metastable flat film

The above results were obtained for liquid volumes, as measured by the spatial period L and mean film height $\bar{h}$, for which the flat film is unstable. For these values of L no steady profile exists other than pinned drops. As a result beyond depinning the thickness profile must vary in space and time. The situation may be different, however, for situations where the mean thickness corresponds to a metastable flat film, i.e., the locally stable flat film coexists with stable pinned drops, and is separated from them by unstable *nucleation* solutions. This is the situation we focus on in the present section.

In the absence of driving the typical situation on a homogeneous substrate is as shown in figure 3 (dashed line). For $L > L_s$ two branches are present, the upper corresponding to stable drops, and the lower to unstable nucleation solutions. In addition, there is a branch of stable flat states given by $||\delta h|| = 0$ with zero energy. Small heterogeneity with $L_{het} = L$ splits the former solutions into two each, and perturbs the flat state into a corrugated state. Thus, for $\epsilon \neq 0$ there will now be five distinct states, instead of the three states when the primary instability is supercritical. The situation is illustrated in figure 27 which shows the resulting five branches as a function of ϵ for both sinusoidal (figures 27(a) and (b)) and localized (figures 27(c) and (d)) wettability defects.

In a driven system, these solutions annihilate pairwise as the driving strength μ increases. Figure 28 shows that for a sinusoidal wettability pattern with a small ϵ the nucleation branches are the first to disappear, followed at larger μ by the drop-like states. As a result for large μ only the nearly flat state remains. However, when ϵ is larger the larger amplitude nucleation state annihilates the lower drop-like state, reducing the number of solutions at given μ first to three, and then with increasing μ to one (see figure 28(a) for $\epsilon = 0.6$). Indeed when $\epsilon \gtrsim 0.6$ only three solutions are present even in the case with no driving. In contrast, for the localized defect (see figure 28(b)) five solutions are present at given $\epsilon > 0$ not too large (see figure 27(c)), of which the middle two annihilate first as μ increases; the next two can persist to quite large driving strength. However, when $\epsilon > 0$ is large ($\epsilon \gtrsim 2.1$) only three solution branches are present, and the top two annihilate with increasing μ leaving the nearly flat film (not shown).

The most important difference from the case studied in the preceding sections lies therefore in the presence of a stable, almost flat film at larger driving strength. As a result the depinning at the rightmost saddle-node does not automatically lead to a periodic orbit; instead the solution may jump to the stable nearly flat state. In this case the drop does not slide downstream but is adsorbed into a flowing film with a steady surface profile or one that is modulated by surface waves. States of this type are, however, difficult to compute numerically since they are connected to very large values of ϵ and/or μ. For instance, the modulated flat film state and the 'last' nucleation state at $\mu = 0$ annihilate, for the parameters of figure 28(b), at $\epsilon = 2211$! Such large values lie outside the range of validity of evolution equations derived using lubrication theory.

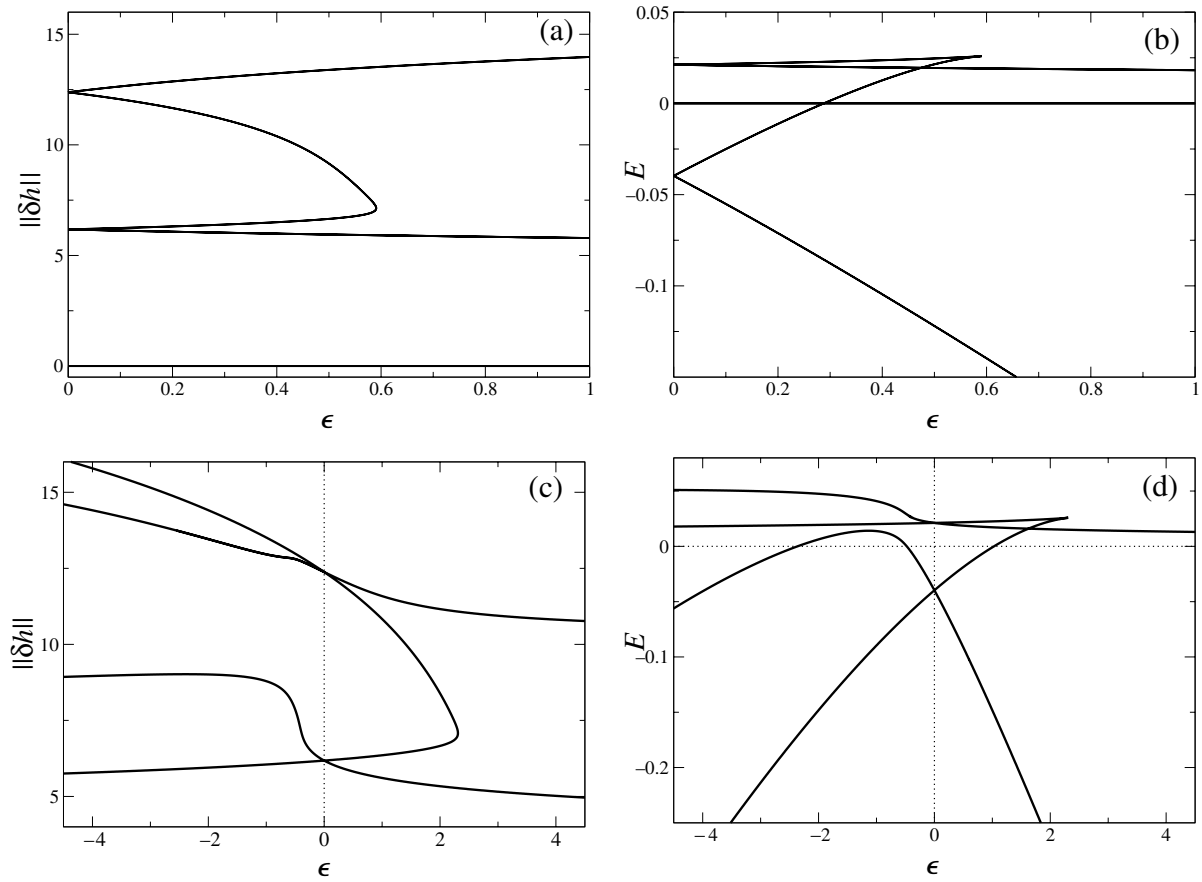

Figure 27. Solution branches on a heterogeneous substrate with no driving for (a), (b) sinusoidal and (c), (d) localized wettability pattern (hydrophobic defect, $s = 6$). When $\epsilon = 0$ the flat film ($||\delta h|| = 0$) coexists stably with the large amplitude drop state (cf figure 3). (a), (c) L^2 norm of δh, and (b), (d) energy E, as functions of the wettability contrast ϵ for $b = 0.1$, $L = 200$ and $\bar{h} = 15$. The spatially modulated flat state is omitted from (c) and (d).

In the present case, however, the above possibility does not arise and one again finds stick-slip motion beyond the saddle-node bifurcation. Figure 29 shows the corresponding bifurcation diagram as a function of μ, while figure 30 shows the position of the drop maximum, the L^2 norm and the profiles as a function of time over slightly more than one period in time. The sharp first peak in the L^2 norm (figure 30(a)) coincides with the accelerating motion due to the passage of the receding contact line over the hydrophobic defect; the main peak arises when the advancing contact line becomes trapped behind the next defect. The small oscillations superposed on the main peak are a numerical artefact related to 'stick-slip' motion on the numerical grid.

7. Conclusions

In this paper, we have explored the process of pinning and depinning of driven drops on heterogeneous substrates. For this purpose, we have formulated the depinning process as a

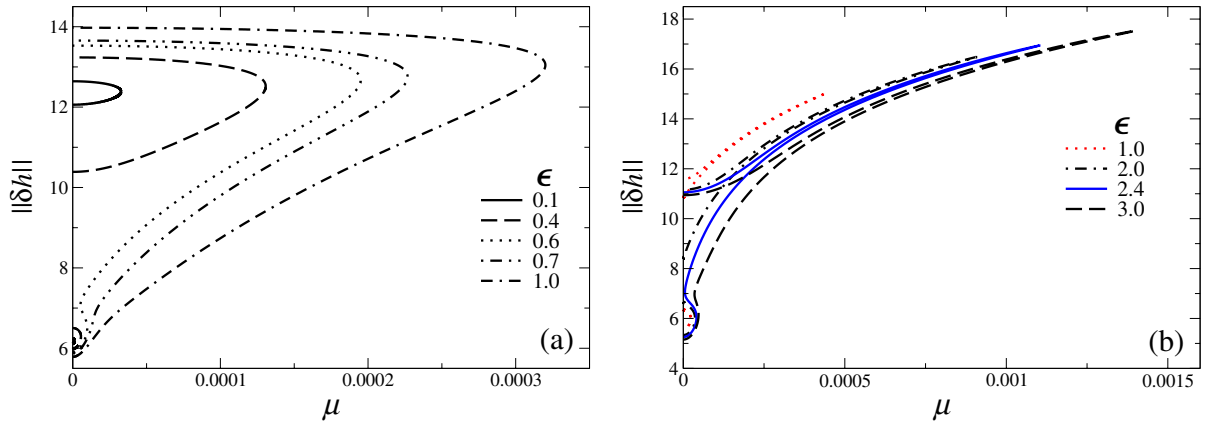

Figure 28. The L^2 norm of stationary solutions as a function of μ for (a) sinusoidal wettability contrast and (b) localized wettability pattern (hydrophobic defect, $s = 6$) when $L = 200$, $b = 0.1$, $\bar{h} = 15$ and various values of ϵ. There is an additional family of solutions at $||\delta h|| \approx 0$ (not shown) corresponding to the metastable flat film.

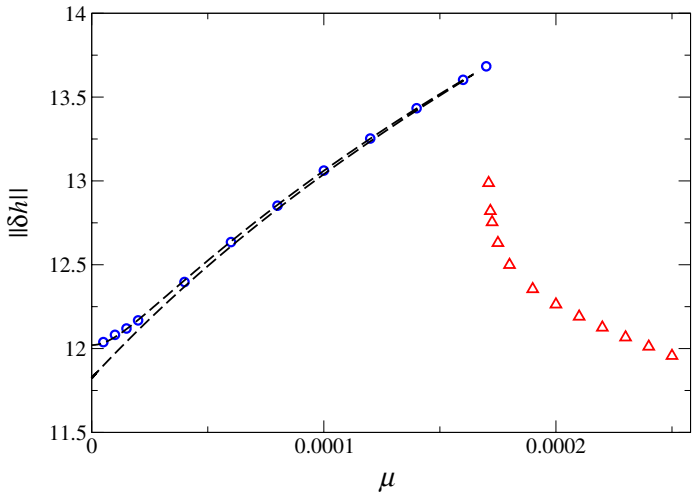

Figure 29. Bifurcation diagram as a function of μ for a localized wettability pattern (hydrophobic defect, $s = 6$, $\epsilon = 0.4$) when $L = 200$, $b = 0.1$, $\bar{h} = 15$, showing the L^2 norm along the branch of steady solutions (– – –) , selected steady solutions obtained by direct integration in time (○) and the time-averaged L^2 norm for the unsteady solutions beyond the depinning bifurcation (△).

bifurcation problem, and focused on a generic problem of this type. This approach permitted us to restrict attention to drops not much thicker than the wetting layer. For simplicity, we considered the case of a heterogeneous interaction between the free interface and substrate with a well-defined spatial period. Such an interaction might arise from spatially varying wetting properties, or heterogeneous temperature or electric fields, while the driving might be caused by gravitational or centrifugal forces, or gradients of wettability, temperature or electric fields. Appendix A lists selected results for a drop pinned in a heterogeneous electric field in a condenser

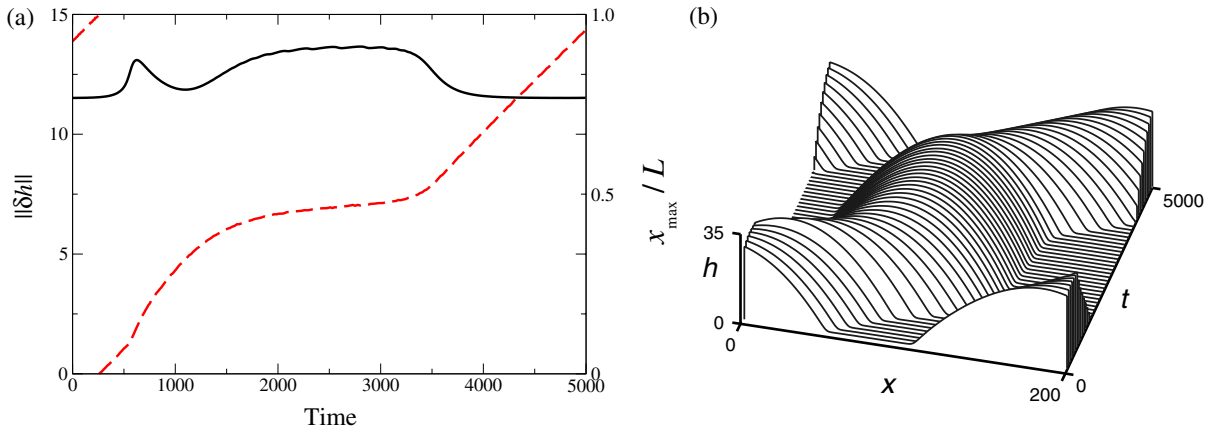

Figure 30. Characteristics of sliding drops beyond depinning from a hydrophobic defect for the parameters of figure 29 and $\mu = 0.00018$. Panel (a) shows the L^2 norm (black solid line; left axis) and the position of the global height maximum (red broken line; right axis) while panel (b) shows the corresponding space-time plot.

that highlights the close resemblance between this system and the generic problem studied in the main body of the paper.

We have examined two types of pinning: pinning by a hydrophilic defect at the back of the drop, and pinning by a hydrophobic defect in front of it, and identified two mechanisms whereby depinning takes place. In the case of a hydrophilic defect the drop stretches markedly just prior to depinning as the driving strength increases; the pinned drop loses stability at a saddle-node bifurcation, resulting in periodic motion as the drop slides over the periodic array of hydrophilic defects. We have referred to this type of bifurcation as the 'sniper'. The periodic motion that results is slow when the drop is stretching, and fast once the drop breaks away from a defect and spills onto the next one. The situation is richer for hydrophobic defects that pin the drop by blocking it. In this case in addition to the steady state sniper bifurcation a new depinning mechanism was observed: the drop loses stability to an oscillatory mode leading to back and forth oscillation of the drop. We believe (but have been unable to demonstrate) that this bifurcation must be supercritical in order to form a homoclinic connection with an unstable drop, and allow the drop to spill over the blocking defect. However, we have been unable to find the (stable) zero-mean oscillations that must be created at such a Hopf bifurcation, possibly because the anticipated global bifurcation occurs very close to the primary Hopf bifurcation. Note that such a Hopf bifurcation is only present because of the flow through the precursor. For larger drops this flow becomes negligible and consequently the dynamics associated with the Hopf bifurcation can only occur for strong defects and very strong driving. The motion that results from oscillatory depinning is in fact very similar to that produced via the sniper bifurcation; the main difference between these two depinning scenarios is confined to behaviour very close to the depinning transition. In the sniper scenario the average speed of the drop vanishes like $(\mu - \mu_c)^{1/2}$, while in the Hopf scenario it drops to zero logarithmically at the global bifurcation separating the rocking motion from sliding. Of course, the average speed at the saddle-node bifurcation that occurs as μ decreases (figure 25(b)) remains finite.

In the paper, we have examined the dependence of the above scenarios on the parameters of the system specifying the profile of the heterogeneity, as well as on the drop volume as measured by the mean thickness $\bar{h}$, and the heterogeneity period L. Not surprisingly we found that for larger volumes depinning occurs for smaller heterogeneity amplitude $|\epsilon|$ (figure 26). This is simply an effect of the weight of the liquid in the drop.

The results of this paper clarify several issues in the theory of liquid films within the continuum lubrication description. On a homogeneous substrate the use of a disjoining pressure defines the mesoscopic contact angle; this is the contact angle that is measured in a laboratory setting. This angle is not specified a priori in the theory, and can only be determined by solving the liquid film equation. As a consequence the downstream and upstream contact angles in driven systems are in general different. Since the problem posed on a homogeneous substrate is invariant under translations, generic spontaneous symmetry-breaking (i.e., drop-forming) instabilities are necessarily Hopf bifurcations and lead to travelling (i.e., sliding) drops. Thus on a homogeneous substrate all nonuniform states slide with respect to the substrate, and one concludes that the precursor film formulation of the problem does not permit pinned drops under lateral driving [2, 52]. In other approaches the precursor is absent and the downstream contact line location and angle is specified *a priori*. Such theories are singular in the sense that the film thickness vanishes outside of the drop, and it is this singularity that mathematically speaking violates the theorem and permits stationary drops. In our formulation such singularities are absent and we must rely on heterogeneities to pin driven drops. In this paper, we have examined in detail the processes that lead to such pinning, as well as the processes that lead to depinning as the strength of the driving is progressively increased. It is unclear to us how depinning would be described within theories that prescribe the contact line.

Although our results are applicable, in principle, to a wide spectrum of systems, in some of these the required parameter values may be hard to realize experimentally. The spectrum of possible applications ranges from (i) nano-drops on ultrathin precursor films of thicknesses $l \approx 1 \ldots 10\,\mathrm{nm}$ where the film-substrate interaction is dominated by wettability (i.e., a disjoining pressure) to (ii) micro-drops on macroscopic wetting layers with $l \approx 10 \ldots 100\,\mu\mathrm{m}$. In the latter case the film-substrate interaction may combine repulsive van der Waals interactions and the influence of temperature and/or electric fields [23, 51, 52]. In principle, the spatial modulation responsible for pinning can be present in any part of this interaction. We estimate the non-dimensional driving force μ using equation (3) based on the wetting layer thickness l and the typical energy density $\kappa = A/l^3$ for a film of thickness l, where A is the Hamaker constant characterizing the van der Waals interaction (note that at the wetting layer thickness the typical energy densities of the two antagonistic terms are roughly equal). For a droplet on a substrate inclined at a (small) angle α to horizontal $\mu = l^5\,\gamma^{1/2}\,A^{-3/2}\,\tilde{\mu}$ (see equation (3)), where $\tilde{\mu} = \rho g \alpha \approx 10^4 \alpha\,\mathrm{N/m^3}$, $A \approx 10^{-20}\,\mathrm{Nm}$ and $\gamma \approx 10^{-1}\,\mathrm{N/m}$, we find that $\mu = l^5\,10^{33}\alpha\,\mathrm{m^{-5}}$. Thus for $l = 1\,\mathrm{nm}, 10\,\mathrm{nm}, 100\,\mathrm{nm}$ and $1\,\mu\mathrm{m}$ the quantity μ/α is $10^{-12}, 10^{-7}, 10^{-2}$ and 10^3, respectively. This result should be compared with the typical value $\mu \approx 10^{-2}$ at the transition between the two types of depinning from the heterogeneities considered in this paper. It follows that gravity-driven depinning via a Hopf bifurcation can only be observed for wetting layer thickness of about 100 nm or more, i.e., in case (ii). A specific example is given in appendix A. In case (i) gravity-driven depinning of droplets will always take place via a sniper bifurcation.

Acknowledgments

This study was supported by NASA, NSF and EU under grants NNC04GA47G (EK and UT), DMS-0305968 (EK) and MRTN-CT-2004-005728 (UT). We are grateful to the organizers of the Isaac Newton Institute program on Pattern Formation in Large Domains for invitations to the Institute where part of this work was done. We thank Karin John for providing us with a time-stepping code that we have adapted to the present problem.

Appendix A. Dielectric liquid in a condenser

In this appendix, we present selected results for a drop of dielectric liquid in a condenser of gap width d. The drop is pinned by a spatial heterogeneity. The evolution equation for the thickness profile $h(x, t)$ of a film of dielectric liquid of relative permittivity ε in air (relative permittivity equal to one) can be derived from the general two-layer result in [23]. In the nondimensional variables used in the body of the paper the equation for $h(x, t)$ is

$$\partial_t h = -\partial_x\{h^3[\partial_x(\partial_{xx}h + P(h, x)) + \mu]\}. \tag{A.1}$$

The pressure $P(h, x)$ contains van der Waals interactions with both condenser walls and the electrostatic pressure. The heterogeneity is assumed to be in the electric field only, i.e.,

$$P(h, x) = [p_{\mathrm{vdW}}^{\mathrm{up}} + p_{\mathrm{vdW}}^{\mathrm{low}} + b(1 + \epsilon\xi(x))p_{\mathrm{el}}]. \tag{A.2}$$

The disjoining pressure models wetting interactions that prevent rupture of the liquid film at the lower plate and rupture of the air film at the upper plate, respectively. We have

$$p_{\mathrm{vdW}}^{\mathrm{low}} = \frac{1}{h^3}, \tag{A.3}$$

$$p_{\mathrm{vdW}}^{\mathrm{up}} = -\frac{1}{(d-h)^3}. \tag{A.4}$$

For simplicity we assume these to be of equal strength. As in the main body of the paper we base the energy density scale κ on van der Waals interactions, i.e., $\kappa = A/l^3$ for wetting layer thickness l.

For a vertical electric field and a layer of dielectric liquid of permittivity ε under air the dimensional vertical field components in the liquid and the air are

$$E_{\mathrm{liq}} = \frac{U}{h + \varepsilon(d-h)} \tag{A.5}$$

and

$$E_{\mathrm{air}} = \frac{\varepsilon U}{h + \varepsilon(d-h)}, \tag{A.6}$$

respectively. In the lubrication approximation the horizontal components can be neglected. The dimensional electrostatic pressure $\tilde{p}_{\mathrm{el}} \equiv \varepsilon_0(\varepsilon - 1)E_{\mathrm{liq}}E_{\mathrm{air}}$ [21, 23], where ε_0 denotes the permittivity of vacuum, provides the dimensionless pressure

$$p_{\mathrm{el}} = \frac{1}{[h + \varepsilon(d-h)]^2} \tag{A.7}$$

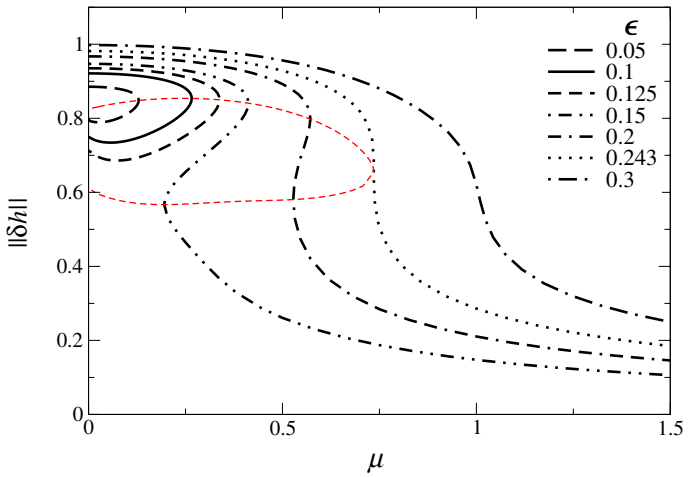

Figure A.1. The L^2 norm of steady solutions in a heterogeneous condenser as a function of the applied driving μ for different heterogeneity amplitudes ϵ as given in the legend, and $L = 10$, $b = 200$, $\bar{h} = 1.5$, $d = 4$. The heterogeneity is given by equation (6) with $s = 6$. The thin dashed line indicates the locus of the two saddle-node bifurcations. The fold at $\mu \approx 0.75$ indicates the transition from depinning via a sniper to depinning via Hopf bifurcation.

and the dimensionless relative interaction strength

$$b = \frac{\varepsilon_0 \varepsilon(\varepsilon - 1)U^2}{2l^2\kappa}, \tag{A.8}$$

where $\varepsilon > 1$. The direction of the applied voltage has no influence on the result.

With $\varepsilon = 2$ (a typical value for silicon oil [23]) and the estimate for κ from section 7 the relative interaction strength is $b = 10^9\, U^2 l\, \mathrm{V}^{-2}\, \mathrm{m}^{-1}$, i.e., for wetting layer thickness between $l = 100\,\mathrm{nm}$ and $1\,\mu\mathrm{m}$ and $U = 1\,\mathrm{V}$, b is in the range 100–1000. Figure A.1 shows a family of steady solutions for $b = 200$. The transition between depinning via sniper and depinning via Hopf bifurcation occurs at a driving strength $\mu \approx 1$, well in the range of gravitational driving. This is also the case for two layers of immiscible liquids of different permittivities and viscosities.

References

[1] Podgorski T, Flesselles J-M and Limat L 2001 Corners, cusps, and pearls in running drops *Phys. Rev. Lett.* **87** 036102

[2] Thiele U, Velarde M G, Neuffer K, Bestehorn M and Pomeau Y 2001 Sliding drops in the diffuse interface model coupled to hydrodynamics *Phys. Rev.* E **64** 061601

[3] Le Grand N, Daerr A and Limat L 2005 Shape and motion of drops sliding down an inclined plane *J. Fluid Mech.* **541** 293–315

[4] Brzoska J B, Brochard-Wyart F and Rondelez F 1993 Motions of droplets on hydrophobic model surfaces induced by thermal gradients *Langmuir* **9** 2220–4

[5] Brochard F 1989 Motions of droplets on solid surfaces induced by chemical or thermal gradients *Langmuir* **5** 432–8

[6] Raphaël E 1988 Spreading of droplets on a patchy surface *C. R. Acad. Sci. Ser. II* **306** 751–4
[7] Chaudhury M K and Whitesides G M 1992 How to make water run uphill *Science* **256** 1539–41
[8] Schwartz L W and Eley R R 1998 Simulation of droplet motion on low-energy and heterogeneous surfaces *J. Colloid Interface Sci.* **202** 173–88
[9] Pismen L M and Thiele U 2006 Asymptotic theory for a moving droplet driven by a wettability gradient *Phys. Fluids* **18** 042104
[10] Joanny J F and de Gennes P-G 1984 A model for contact angle hysteresis *J. Chem. Phys.* **81** 552–62
[11] Israelachvili J N and Gee M L 1989 Contact angles on chemically heterogeneous surfaces *Langmuir* **5** 288–9
[12] Schwartz L W and Garoff S 1985 Contact angle hysteresis on heterogeneous surfaces *Langmuir* **1** 219–30
[13] Schwartz L W 1998 Hysteretic effects in droplet motions on heterogeneous substrates: direct numerical simulation *Langmuir* **14** 3440–53
[14] Nadkarni G D and Garoff S 1994 Reproducibility of contact line motion on surfaces exhibiting contact angle hysteresis *Langmuir* **10** 1618–23
[15] Decker E L and Garoff S 1996 Using vibrational noise to probe energy barriers producing contact angle hysteresis *Langmuir* **12** 2100–10
[16] Marmur A 1996 Equilibrium contact angles: theory and measurement *Colloid Surf. A: Physicochem. Eng. Asp.* **116** 55–61
[17] Brandon S and Marmur A 1996 Simulation of contact angle hysteresis on chemically heterogeneous surfaces *J. Colloid Interface Sci.* **183** 351–5
[18] Collet P, De Coninck J, Dunlop F and Regnard A 1997 Dynamics of the contact line: Contact angle hysteresis *Phys. Rev. Lett.* **79** 3704–7
[19] Burelbach J P, Bankoff S G and Davis S H 1990 Steady thermocapillary flows of thin liquid layers. II. Experiment *Phys. Fluids* A **2** 321–33
[20] Kabov O A 1998 Formation of regular structures in a falling liquid film upon local heating *Thermophys. Aeromech.* **5** 547–51
[21] Lin Z, Kerle T, Baker S M, Hoagland D A, Schäffer E, Steiner U and Russell T P 2001 Electric field induced instabilities at liquid/liquid interfaces *J. Chem. Phys.* **114** 2377–81
[22] Morariu M D, Voicu N E, Schäffer E, Lin Z, Russell T P and Steiner U 2003 Hierarchical structure formation and pattern replication induced by an electric field *Nature Mater.* **2** 48–52
[23] Merkt D, Pototsky A, Bestehorn M and Thiele U 2005 Long-wave theory of bounded two-layer films with a free liquid–liquid interface: short- and long-time evolution *Phys. Fluids* **17** 064104
[24] Joanny J F and Robbins M O 1990 Motion of a contact line on a heterogeneous surface *J. Chem. Phys.* **92** 3206–12
[25] Quéré D, Azzopardi M J and Delattre L 1998 Drops at rest on a tilted plane *Langmuir* **14** 2213–6
[26] Schäffer E and Wong P Z 2000 Contact line dynamics near the pinning threshold: a capillary rise and fall experiment *Phys. Rev.* E **61** 5257–77
[27] Roura P and Fort J 2001 Equilibrium of drops on inclined hydrophilic surfaces *Phys. Rev.* E **64** 011601
[28] Rehse N, Wang C, Hund M, Geoghegan M, Magerle R and Krausch G 2001 Stability of thin polymer films on a corrugated substrate *Eur. Phys. J.* E **4** 69–76
[29] Brusch L, Kühne H, Thiele U and Bär M 2002 Dewetting of thin films on heterogeneous substrates: pinning vs. coarsening *Phys. Rev.* E **66** 011602
[30] Thiele U, Brusch L, Bestehorn M and Bär M 2003 Modelling thin-film dewetting on structured substrates and templates: bifurcation analysis and numerical simulations *Eur. Phys. J.* E **11** 255–71
[31] Dussan E B 1979 On the spreading of liquids on solid surfaces: static and dynamic contact lines *Annu. Rev. Fluid Mech.* **11** 371–400
[32] de Gennes P-G 1985 Wetting: statistics and dynamics *Rev. Mod. Phys.* **57** 827–63
[33] Leger L and Joanny J F 1992 Liquid spreading *Rep. Prog. Phys.* **55** 431–86
[34] Robbins M O and Joanny J F 1987 Contact-angle hysteresis on random surfaces *Europhys. Lett.* **3** 729–35
[35] Ertas D and Kardar M 1994 Critical dynamics of contact line depinning *Phys. Rev.* E **49** R2532–R2535

[36] Golestanian R and Raphaël E 2001 Relaxation of a moving contact line and the Landau–Levich effect *Europhys. Lett.* **55** 228–34
[37] Schäffer E and Wong P Z 1998 Dynamics of contact line pinning in capillary rise and fall *Phys. Rev. Lett.* **80** 3069–72
[38] Tavana H, Yang G C, Yip C M, Appelhans D, Zschoche S, Grundke K, Hair M L and Neumann A W 2006 Stick-slip of the three-phase line in measurements of dynamic contact angles *Langmuir* **22** 628–36
[39] Starov V M 1992 Equilibrium and hysteresis contact angles *Adv. Colloid Interface Sci.* **39** 147–73
[40] Adler R 1946 A study of locking phenomena in oscillators *Proc. I.R.E. Waves Electrons* **34** 351–7
[41] Strogatz S H 1994 *Nonlinear Dynamics and Chaos* (Reading, MA: Addison-Wesley)
[42] Coullet P, Goldstein R E and Gunaratne G H 1989 Parity-breaking transitions of modulated patterns in hydrodynamic systems *Phys. Rev. Lett.* **63** 1954–7
[43] Dangelmayr G, Hettel J and Knobloch E 1997 Parity-breaking bifurcation in inhomogeneous systems *Nonlinearity* **10** 1093–114
[44] Sanders J A and Cushman R 1986 Limit cycles in the Josephson equation *SIAM J. Math. Anal.* **17** 495–511
[45] Siggers J H 2003 Dynamics of target patterns in low-Prandtl-number convection *J. Fluid Mech.* **475** 357–75
[46] Aranson I S, Malomed B A, Pismen L M and Tsimring L S 2000 Crystallization kinetics and self-induced pinning in cellular patterns *Phys. Rev.* E **62** R5–R8
[47] Burke J and Knobloch E 2006 Localized states in the generalized Swift–Hohenberg equation *Phys. Rev.* E **73** 056211
[48] Oron A, Davis S H and Bankoff S G 1997 Long-scale evolution of thin liquid films *Rev. Mod. Phys.* **69** 931–80
[49] Le Doussal P, Wiese K J, Raphaël E and Golestanian R 2006 Can nonlinear elasticity explain contact-line roughness at depinning? *Phys. Rev. Lett.* **96** 015702
[50] Oron A and Rosenau P 1992 Formation of patterns induced by thermocapillarity and gravity *J. Physique II France* **2** 131–46
[51] Bestehorn M, Pototsky A and Thiele U 2003 3D large scale Marangoni convection in liquid films *Eur. Phys. J.* B **33** 457–67
[52] Thiele U and Knobloch E 2004 Thin liquid films on a slightly inclined heated plate *Physica* D **190** 213–48
[53] Sharma A 1993 Relationship of thin film stability and morphology to macroscopic parameters of wetting in the apolar and polar systems *Langmuir* **9** 861–9
[54] Thiele U, Neuffer K, Pomeau Y and Velarde M G 2002 On the importance of nucleation solutions for the rupture of thin liquid films *Colloid Surf.* A **206** 135–55
[55] Israelachvili J N 1992 *Intermolecular and Surface Forces* (London: Academic)
[56] Teletzke G F, Davis H T and Scriven L E 1988 Wetting hydrodynamics *Rev. Phys. Appl.* **23** 989–1007
[57] Thiele U, Velarde M G and Neuffer K 2001 Dewetting: film rupture by nucleation in the spinodal regime *Phys. Rev. Lett.* **87** 016104
[58] Sharma A and Khanna R 1998 Pattern formation in unstable thin liquid films *Phys. Rev. Lett.* **81** 3463–6
[59] Sharma A and Khanna R 1999 Pattern formation in unstable thin liquid films under the influence of antagonistic short- and long-range forces *J. Chem. Phys.* **110** 4929–36
[60] Thiele U, Velarde M G, Neuffer K and Pomeau Y 2001 Film rupture in the diffuse interface model coupled to hydrodynamics *Phys. Rev.* E **64** 031602
[61] Becker J, Grün G, Seemann R, Mantz H, Jacobs K, Mecke K R and Blossey R 2003 Complex dewetting scenarios captured by thin-film models *Nature Mater.* **2** 59–63
[62] Thiele U, John K and Bär M 2004 Dynamical model for chemically driven running droplets *Phys. Rev. Lett.* **93** 027802
[63] John K, Bär M and Thiele U 2005 Self-propelled running droplets on solid substrates driven by chemical reactions *Eur. Phys. J.* E **18** 183–99
[64] Pismen L M 2006 Perturbation theory for traveling droplets *Phys. Rev.* E **74** 041605
[65] Spaid M A and Homsy G M 1996 Stability of Newtonian and viscoelastic dynamic contact lines *Phys. Fluids* **8** 460–78

[66] Moyle D T, Chen M-S and Homsy G M 1999 Nonlinear rivulet dynamics during unstable wetting flows *Int. J. Multiphase Flow* **25** 1243–62

[67] Pismen L M and Pomeau Y 2000 Disjoining potential and spreading of thin liquid layers in the diffuse interface model coupled to hydrodynamics *Phys. Rev.* E **62** 2480–92

[68] Thiele U, Neuffer K, Bestehorn M, Pomeau Y and Velarde M G 2002 Sliding drops on an inclined plane *Colloid Surf.* A **206** 87–104

[69] Thiele U and Knobloch E 2003 Front and back instability of a liquid film on a slightly inclined plate *Phys. Fluids* **15** 892–907

[70] NAG c library, Mark 6, 2000 Online at www.nag.co.uk

[71] Dangelmayr G and Knobloch E 1987 The Takens–Bogdanov bifurcation with O(2)-symmetry *Phil. Trans. R. Soc. Lond. A: Math. Phys. Eng. Sci.* **322** 243–79